COMPARISON OF METHODS FOR THERMOACOUSTIC STABILITY ANALYSIS OF A HYDROGEN-FUELLED CONDENSING BOILER

MARC SHAIR ALI
October, 2024

SUPERVISORS:

Dr.ir. J.B.W. Kok

ir. J.W. Hofsteenge
Dr.ir. N.A. Beishuizen

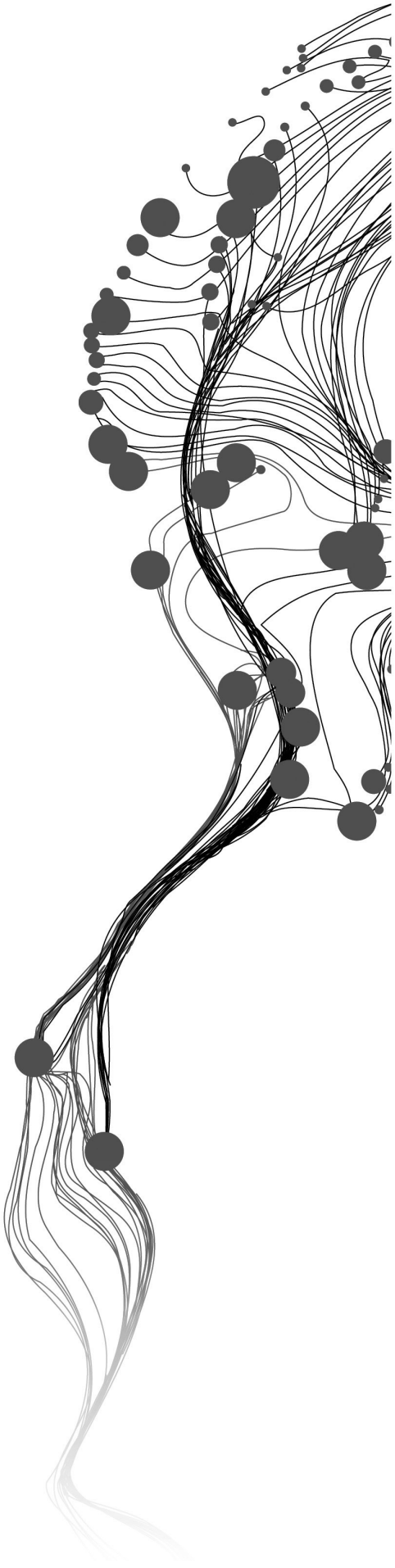

COMPARISON OF METHODS FOR THERMOACOUSTIC STABILITY ANALYSIS OF A HYDROGEN-FUELLED CONDENSING BOILER

MARC SHAIR ALI
Enschede, The Netherlands, October, 2024

Specialization: ME-Energy & Flow

Chair: Thermal Engineering
University of Twente

SUPERVISORS:

Dr.ir. J.B.W. Kok

ir. J.W. Hofsteenge
Dr.ir. N.A. Beishuizen

THESIS ASSESSMENT BOARD:

Dr.ir. J.B.W. Kok (chair)

Dr. M. Mehrali (internal member)

Dr.ir. J.A.M. Withag (external member)

ir. J.W. Hofsteenge (supervisor)
Dr.ir. N.A. Beishuizen (mentor from company)

ABSTRACT

Thermoacoustic instability is a combustor pressure oscillation due to feedback of unsteady heat release of a flame and acoustic perturbations. This feedback can cause premature failure of systems. Due to fast chemical kinetics in hydrogen combustion as compared to natural gas, a hydrogen-fuelled system is likely to be more sensitive to thermoacoustic instability. Conventionally this instability is analyzed with transient CFD simulation of the combustion process. In this work, a residential hydrogen-fuelled condensing boiler is analyzed. This study compares methods to determine the Flame Transfer Function (FTF), a function describing the effect of the flame on the heat release due to a flow perturbation (equivalence ratio perturbations in this work). This thesis work is performed as part of the 'combustion DYNamics and Acoustics oscillations in large industrial Furnaces and boilers' (DYNAF) project. For large scale boilers, transient simulations can be more expensive due to the large time and length scales involved. The development of a steady state based method to replace these simulations is interesting to determine with modest effort thermoacoustic stability in the design process of the burners.

Two transient methods, impulse excitation and white noise excitation, are compared to a steady state method, the Linear Coefficient Method (LCM), to evaluate computational expense and accuracy. The FTF is determined for the hydrogen-fuelled condensing boiler. The Finite Rate/Eddy Dissipation Model (FR/EDM) is compared to the UT-Flamelet Generated Manifold (UT-FGM) combustion model. The FTF is determined using the different methods and implemented in an Acoustic Network Model (ANM) of the condensing boiler to determine thermoacoustic stability.

Speed improvements have been made to the LCM such that the computation time is low compared to the transient methods for the case study. The used implementation of the LCM did not give accurate results. The transient methods showed good agreement in the FTF. A peak in the gain at $St \approx 1$ is observed which is a direct result of the excitations applied to the transient simulations. The eigenfrequencies of the system as found using the ANM are similar. The analyzed condensing boiler is stable.

Keywords

Combustion, Hydrogen, Thermoacoustic stability, Acoustic network model

ACKNOWLEDGEMENTS

Several people have aided me over the past months of my Master's thesis. I would like to thank my supervisors, Jim Kok and Nijso Beishuizen, for the support and feedback during my project. The weekly and biweekly meetings with them where I could ask questions and get feedback were extremely beneficial. I would especially like to thank my daily supervisor Jesse Hofsteenge for the amazing supervision, great help and good chats during my Master's project. His help with brainstorming and problem solving has been indispensable. In addition, all the valuable insight he provided have fundamentally shaped this research.

Furthermore, I want to thank family and friends for the support over the past months. The much needed breaks and relaxation they provided helped tremendously. Having them as an outlet for occasional frustrations has helped as well. Here I want to thank my housemates in particular who supported me with 'Engineering Juice' (Coffee) and facilitating 'Rubber duck debugging.'

TABLE OF CONTENTS

Chapter 1

Introduction

International policy is driving a shift to sustainable sources such as hydrogen. In residential appliances, a point of focus of the research has been blending natural gas with a volume fraction of hydrogen. Hydrogen volume fractions up to 20% allow most appliances to function without issue [8, 20, 23]. Higher percentages can lead to problems such as flashback. This flame stability issue can cause flame extinction leading to spillage of the combustible mixture [5]. To prevent this safety issue while allowing increased hydrogen contents in the fuel supply, new appliances need to be developed to work on a 100% hydrogen fuel source. The notion for the Dutch government as developed by NEN (Nederlands Normalisatie Instituut) is to construct a transport network for high purity hydrogen, rather than focusing on blended natural gas [37].

Different problems arise in the development of a hydrogen (residential) appliance. Due to the higher laminar flame speed of hydrogen as compared to natural gas, flashback and flame holding are more prevalent problems. More significant for this work is the thermoacoustic behaviour of hydrogen flames. Thermoacoustic instability is a combustor pressure oscillation due to feedback of the unsteady heat release of a flame and the acoustic response of the system (see Chapter 2). Due to fast chemical kinetics in hydrogen combustion, a hydrogen-fuelled system is likely to be more sensitive to thermoacoustic instability [36]. A study by Kang and Kim [18] on a multi-element burner found hydrogen-air flames can have 12kPa pressure fluctuations resulting from Heat Release Rate (HRR) perturbations less than 1%. Combining these pressure fluctuations with the increase in intrinsic thermoacoustic mode frequency for increasing hydrogen content in the fuel [7] can cause a system to fail more quickly compared to methane-air systems. As such, the thermoacoustic stability analysis is important in the design of a hydrogen burning system.

1.1 PROBLEM STATEMENT

Different numerical methods exist for a thermoacoustic stability analysis. These methods focus on determining a Flame Transfer Function (FTF; see Chapter 3). The FTF is generally obtained by measuring the response of the system in time to an excitation. As a result, these methods require transient Computational Fluid Dynamics (CFD) simulations to be performed. Alternatively, the FTF can be determined with steady state methods [4, 38], although the use of these tools does not seem wide-spread. A knowledge gap is present regarding these steady state methods with hydrogen combustion.

In this work, the Linear Coefficients Method (LCM; see Chapter 3.2) developed at the University of Twente by J.F. Van Kampen [38] is tested on hydrogen combustion simulations. This

steady state method of determining the FTF is compared to 2 transient methods, to determine the resulting computation time and accuracy. The FTF is determined for a residential hydrogen-fuelled condensing boiler developed by Nefit|Bosch Thermotechniek B.V. (Section 1.4).

This thesis work is performed as part of the 'combustion DYNamics and Acoustics oscillations in large industrial Furnaces and boilers' (DYNAF) project, funded by the Dutch Research Council (NWO) in the Open Technology Program. For large scale boilers, transient simulations can be more expensive due to the large time and length scales involved. The development of a steady state methods to replace these simulations is interesting to determine thermoacoustic stability in the design process of the burners.

1.2 RESEARCH QUESTION

While the main goal is determining thermoacoustic stability of the hydrogen-fuelled residential condensing boiler, the research will compare methods of performing this analysis which could advance the development of steady state based methods. Consequently, this leads to the main research question:

> *To what extent can the LCM improve computation time and accuracy compared to white noise or impulse excitation in determining thermoacoustic stability in a hydrogen burning residential appliance?*

The research subquestions to obtain an answer to this main question are:

- Can the UT-FGM combustion model be used?
- Do LCM, white noise and impulse excitation result in similar thermoacoustic eigenfrequencies?

1.3 SCOPE

The scope of the research is limited to (U)RaNS simulations of (pure) hydrogen-air mixtures. Steady state solutions will be used as initial conditions for determining the FTFs. The $k-\varepsilon$ turbulence model will be used for the final simulations (to obtain the steady state solutions and in the transient simulations of the combustion chamber). Adiabatic wall conditions will be considered for determining the FTFs. The domain in the CFD simulations starts from the air and hydrogen inlets up to the heat exchanger. The heat exchanger is not analyzed; a temperature boundary condition will be applied to approximate the heat loss. NO_X-emissions will not be considered in this work.

1.4 CASE STUDY

The residential appliance examined in this work is a hydrogen-fuelled residential condensing boiler developed by Nefit|Bosch Thermotechniek B.V. Figure 1.1 shows an example of such a boiler. Air

enters through the gas inlet where a fan is located. The fuel mixes with the air in the mixing chamber before the burner wall. The flame extends radially outward to the coil heat exchanger. The mixing chamber and combustion chamber are cylindrical and contain periodic features.

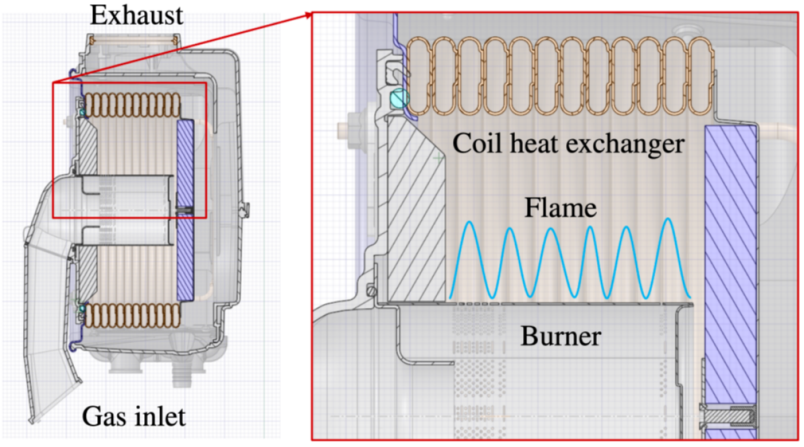

Figure 1.1: Schematic cross-section of a residential condensing boiler courtesy of Nefit|Bosch Thermotechniek B.V. The design of this boiler is similar to the system investigated in this work.

These appliances generally have power requirements in the order of 25kW [29]. The hydrogen combustion is lean; in other words, the equivalence ratio ϕ_{design} is less than unity. The choice in equivalence ratio is a balance between efficiency and emissions: A very lean flame will have low NO_X-emissions, as the flame temperature is reduced. More energy is expended in heating the superfluous air that leaves the combustion chamber, such that the efficiency of the system is reduced. Conversely, a flame near stoichiometric conditions ($\phi_{st} = 1$) will have a higher efficiency, but NO_X-emissions will increase.

The residential condensing boiler examined in this work is characterized by the near-laminar flame distributed on a burner surface. The burner wall is a thin metal plate with perforations for the combusting mixture to pass through. In the combustion chamber, these perforations act to distribute the flame over a wide area and to anchor the flame. As this is a residential appliance, noise production needs to be limited. A highly turbulent flame will have excessive noise, which would require more sound insulation to be added to the design.

For reasons of confidentiality, exact dimensions and specifications of the system are omitted. Figures showing dimensions are either normalized or distorted. All dimensions will be made non-dimensional in the following way:

- Frequency f: A frequency relevant to the flame will be made non-dimensional using the Strouhal number:

$$St = \frac{fL}{U} \tag{1.1}$$

  This number uses a characteristic length L and velocity U to scale the frequency. In this work, the length is the flame length and the velocity is the mean velocity u_0 of the flow at the inlet of the combustion chamber.

- Length x: Length scales are normalized with the thermal flame thickness computed using

Equation 4.21:

$$\overline{x} = \frac{x}{\delta_L^0} \tag{1.2}$$

In terms of grid length, a normalized length scale of 1 means the entire (thermal) flame thickness fits inside 1 grid element. $\overline{x} >> 1$ for grid elements result in elements larger than the flame thickness.

- Temperature T: Temperature is normalized by the adiabatic flame temperature given the design equivalence ratio ϕ_{design} (starting from normal conditions).

$$\overline{T} = \frac{T}{T_{design}} \tag{1.3}$$

- Time t: Time is non-dimensionalized using the same characteristic scales L and U as the frequency, as:

$$\overline{t} = \frac{tU}{L} \tag{1.4}$$

This normalized time describes the number of periods with characteristic frequency U/L.

Chapter 2

Thermoacoustic stability

Thermoacoustics is the interaction between a heat source and acoustic waves. Two main phenomena can occur resulting from the coupling of these processes in combustion systems [32]: combustion noise and combustion instabilities. Combustion noise is a one-way coupling of a flame with acoustic waves. Thermoacoustic instability follows from a two-way coupling of a heat source and the sound waves. Unsteady heat release from a flame produces acoustic waves that travel through the system. These waves can be reflected (partially) by the geometry of the system to propagate back to the flame front and further upstream. The acoustic waves perturb the HRR of the flame, which in turn can alter the acoustic waves produced [43]. When the acoustic pressure perturbations are within 90° of the unsteady HRR perturbations, the pressure fluctuations intensify. This amplitude grows until non-linearities influence the process. The system reaches a limit cycle where high pressure fluctuations occur at a high frequency. This can lead to adverse effects such as premature failure of the system due to fatigue of the construction.

An example of instabilities in combustion is the Saturn V's F-1 rocket engine. During the development of the engine, the manufacturer Rocketdyne ran into combustion instabilities with chamber pressures exceeding design limits [42]. Part of the injectors eroded from burning as a result. The method used to resolve the instability involved altering the injector design to include an array of baffles. This change in geometry prevented the self-excitation in the combustion.

For a more comprehensive understanding of thermoacoustic (in)stability, the reader is referred to sources such as [24, 32, 38, 43]. This work assumes the reader is familiar with the basics of the two-way coupling mechanism between heat sources (reacting flows) and acoustic waves. To perform the stability analysis, simulation of the self-exciting feedback loop is split into two processes: CFD analysis to find the relation between mixture perturbations and heat release oscillations; and acoustic modelling to find the acoustic response. A CFD simulation of the complete combustion instability feedback (see Figure 2.1(a)) is not feasible for this work due to the time scales involved. While flow perturbations (such as a mixture fraction perturbation) travel with the flow speed, acoustic waves travel with the local speed of sound. For low Mach number flows, as is the case for the residential appliance examined in this work, this difference in time scales would slow down the simulation excessively. Rather, the CFD simulation is used to obtain an FTF, a function describing the heat release response of the flame as a function of a flow perturbation. This FTF is then used to simulate the acoustic response using an Acoustic Network Model (ANM). The combination of these methods is the forced combustion process examined in this work (see Figure 2.1(b)). The method of obtaining the FTF is discussed in Chapter 3 more extensively.

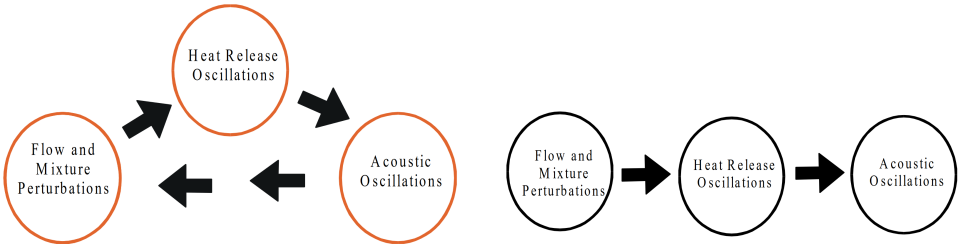

(a) Self-exciting feedback in combustion instability.

(b) Forced combustion used for simulation.

Figure 2.1: Self-exciting feedback versus forced combustion simulation (image from [24])

2.1 ACOUSTIC NETWORK MODEL

To model the acoustic response using an ANM, different source codes are available, such as OSCILOS [27] (Imperial College London) and taX [33] (Technical University of Munich). In this work UTA is used, the ANM code developed at the University of Twente. These three codes are developed in Matlab. For a more detailed background into the ANM code, the reader is referred to [38].

The ANM code solves for pressure perturbations $\boldsymbol{p'}$ as a function of mass flow perturbation $\boldsymbol{M'}$ in the system:

$$\boldsymbol{A}\boldsymbol{p'} = \boldsymbol{M'} \tag{2.1}$$

Here, $\boldsymbol{A}$ is a system matrix containing the linear relations between pressure perturbations and mass flow perturbations for all elements in the network model. Different elements that represent the real geometry are modelled. By coupling these elements, the $\boldsymbol{A}$-matrix can be constructed. The elements are wave number dependent, which in turn makes the $\boldsymbol{A}$-matrix frequency dependent.

An example of an ANM is shown in Figure 2.2. This basic system contains an air inlet at node 1, a separate fuel inlet at node 2 and an outlet at node 5. Acoustic boundary conditions need to be applied at these nodes to close the system. In UTA, reduced impedance ζ boundary conditions can be applied at inlets and outlets. The reduced impedance is a measure of the acoustic effects of all parts downstream of a point [32]:

$$\zeta = \frac{1}{\rho_0 c_0} \frac{p'}{u'} \tag{2.2}$$

Here, ρ_0 and c_0 are the mean flow density and speed of sound, respectively, and p' and u' are the relevant acoustic pressure and velocity perturbations are a point. A duct terminating in a wall has $u' = 0$, resulting in the impedance $\zeta \to \infty$. A duct terminating in a large vessel has an acoustic pressure perturbation $p' = 0$, resulting in the impedance $\zeta = 0$. In addition to impedance boundary conditions, a mass flow perturbation can be applied. This perturbation (in kg/s) is stored in the $\boldsymbol{M'}$-vector.

The ANM can contain a flame element, which loads an FTF obtained from experiments or (CFD) simulations. This flame element can result in singularities for complex frequencies $\omega_r + \omega_i i$ due to the time delay involved in the FTF. These singularities occur at the eigenfrequencies, when $\det(\boldsymbol{A}(\omega_r, \omega_i)) = 0$. ω_r is the frequency of the oscillation that occurs at these singularities. The system is unstable if these frequencies contain an imaginary part $\omega_i < 0$; oscillations will grow in

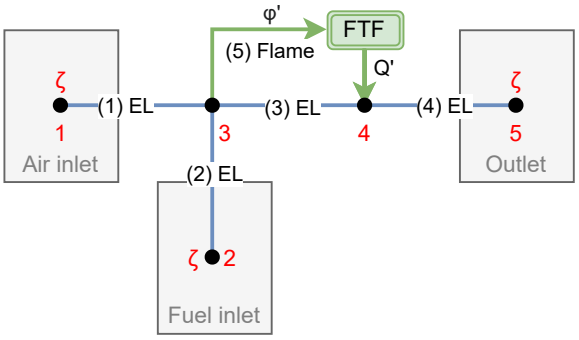

Figure 2.2: Example of an acoustic network model with a flame transfer function (green) implemented (image adapted from [38]). The nodes (black dots with red index) are connected by 1D elements (blue lines with element number and types). Impedance boundary conditions ζ are applied at the inlet (1 and 2) and outlet (5) nodes.

time for these values of ω_i. A growth rate GR can be defined:

$$GR = e^{-2\pi \frac{\omega_i}{\omega_r}} - 1 \tag{2.3}$$

For $GR < 0$, oscillations are damped in time; for $GR > 0$, oscillations grow in time. Consequently, a system that is thermoacoustically stable needs a $GR < 0$ for all frequencies where $\boldsymbol{A}$ is singular.

The ANM-code gives 2 main outputs: the pressure perturbations in the nodes as a function of frequencies; the (imaginary) frequencies for which $|\det(\boldsymbol{A}(\omega_r, \omega_i))| \downarrow 0$. The former is obtained by solving the system for the unknown $\boldsymbol{p'}$. This pressure perturbation can be plotted in a graph (an example is shown in Figure 2.3), to show frequency behaviour resulting from the perturbation. In the stability plot, the eigenfrequencies are shown. Using a local search algorithm, these frequen-

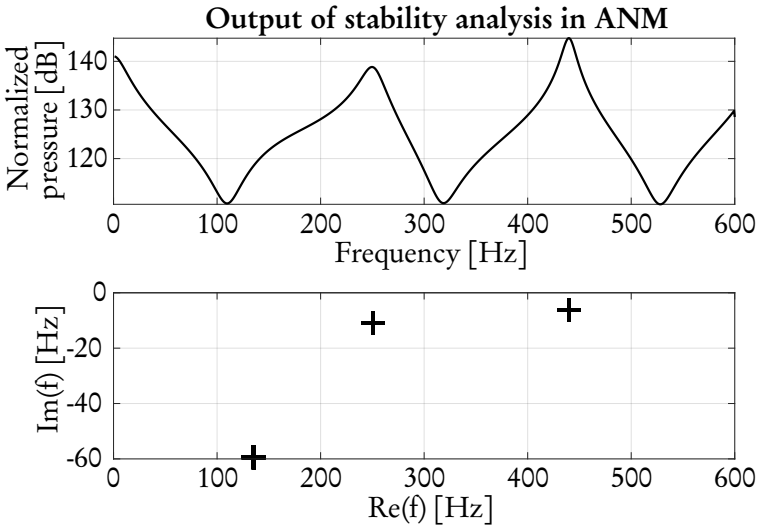

Figure 2.3: Example of output of the acoustic network model for the example acoustic network model in Figure 2.2. The pressure perturbation (top) and stability (bottom) plots are shown. The eigenfrequencies (crosses in the stability plot) contain $\omega_i < 0$Hz, meaning the system is unstable.

cies can also be identified. The minimization function used is the determinant of the $\boldsymbol{A}$-matrix. As this determinant can be in the order of 10^{-40} for stable frequencies, the objective function is scaled using the $\log(\det(\boldsymbol{A}))$. This does not affect the frequencies for which the matrix is singular. It only changes the magnitude of the determinant for improved minimization.

The minimization algorithm in this work is a simplex search method [21], implemented in matlab in the `fminsearch()`-function. This method is based on the Nelder-Mead algorithm [26], which is a zeroth-order, direct search method. As such, the direct objective function is minimized without computing gradients. This method is a local search method, meaning the choice in initial guess for the solution can influence the result. As such, different initial guesses are required to find all frequencies within the relevant frequency band where $\det(\boldsymbol{A}) \downarrow 0$.

Chapter 3

Flame Transfer Function

This chapter covers the essentials of the Flame Transfer Function (FTF). Section 3.1 discusses transient CFD based methods of determining the FTF. The two transient based methods compared in this work are impulse excitation (Section 3.1.2) and white noise excitation (Section 3.1.1). After, the steady state based Linear Coefficients Method (LCM) is explained (Section 3.2).

The flame behaviour is captured in a function to describe the linear global response of the flame to a flow perturbation. The perturbation can be different parameters such as a velocity perturbation. In this work, the inlet perturbation is an equivalence ratio perturbation ϕ' and the measured global response is the unsteady Heat Release Rate (HRR) $\dot{Q}'$:

$$\frac{\dot{Q}'}{\overline{\dot{Q}}} = \mathrm{FTF}\frac{\phi'}{\overline{\phi}} \tag{3.1}$$

The perturbed values and FTF are frequency dependent. The flames generally behave as a low-pass filter with a linear phase shift for a constant convective time delay [1]. As such, high frequency behaviour is generally damped, though screech has been reported at 1 to 2 kHz as in Kang [18]. For a more detailed explanation of the FTF, the reader is referred to other sources, such as [24, 25, 35, 38].

3.1 TRANSIENT BASED METHODS

The FTF can be determined numerically using a transient based CFD approach. The excitation level applied at the inlet is sufficiently low to prevent excitation of non-linearities. If the signal is too low, the response will be lost in noise of the simulation. Different excitation methods can be used, such as (multi)harmonic excitation, impulse excitation and step-in excitation. In this work, only white noise and impulse excitation are considered for determining the stability of the condensing boiler.

3.1.1 White noise excitation

White noise excitation imposes a noisy distribution on the equivalence ratio input. This perturbation is constantly varied in time following an ideally flat spectrum of excited frequencies. In practice, the value of the fluctuation changes at the sampling rate of the output. Varying the perturbation at every time step in the transient simulation will slow down the simulation and can lead

to a poor signal-to-noise ratio. The signal is generated using a pseudorandom number generator, such as Matlabs `rand( )` function, to generate a uniformly distributed set of random numbers.

White noise excitation results in the best fit for non-linear systems due to the randomness in the excitation and an averaging procedure that filters non-linearities. In addition, the uniform distribution of random numbers results in a low crest factor as energy is well distributed over the entire bandwidth. Consequently, non-linearities are excited less compared to other methods. A disadvantage is the high computational expense due to the averaging procedure.

The excitation is approximately 1% of the mean value to get a good signal-to-noise ratio. Figure 3.1 shows an example of a 1% excitation level used in simulation. The excitation level is constant for 10 time steps to improve the signal-to-noise ratio. The HRR is sampled at sampling frequency

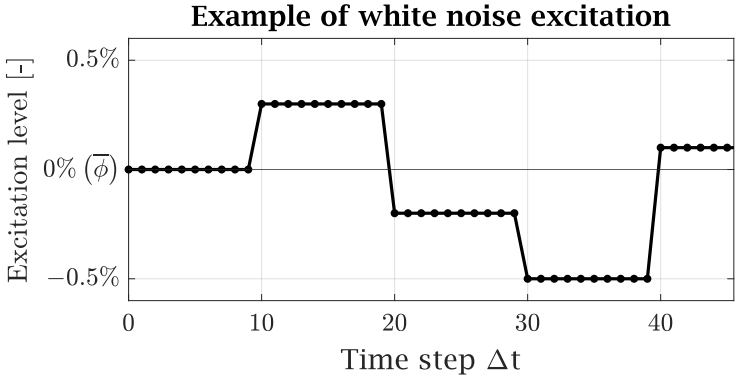

Figure 3.1: Example of a randomly generated excitation for white noise excitation. The markers are the excitations used in the transient CFD simulation. With 1% excitation level, the perturbation varies around the mean value $\overline{\phi}$.

f_s at the start of a new excitation value. The input and response are converted from a time domain signal to a frequency domain signal with a Fast Fourier Transform (FFT). The auto and cross correlations S of these signals are computed using:

$$S_{FX} = FFT(\phi') \cdot \text{conj}(FFT(\dot{Q}')) \tag{3.2}$$

$$S_{FF} = FFT(\phi') \cdot \text{conj}(FFT(\phi')) \tag{3.3}$$

$$S_{XX} = FFT(\dot{Q}') \cdot \text{conj}(FFT(\dot{Q}')) \tag{3.4}$$

Here, the subscript F is for the excitation and X is for the response of the system. conj( ) stands for the complex conjugate of the bracket term. The FTF H_f is then computed with the auto and cross correlation of the excitation:

$$H_f = \frac{S_{FX}}{S_{FF}} \tag{3.5}$$

Due to the random nature of the excitation, an averaging procedure is applied to the auto and cross correlations. The full simulation time is divided into a number of bins with a certain overlap. These two parameters, number of bins and percentage overlap, are tuning parameters for the FTF. They do not change the overall behaviour of the FTF, but they can reduce noise in the transfer function. To reduce the effect of spectral leakage, a windowing function is used (Hanning window in this work). As the excitation is not exactly harmonic in time, the Fourier transformed signal can 'leak' energy to different discrete frequencies [38]. This effect can obscure behaviour, such as low

amplitude peaks. The windowing function rolls off to zero at the extrema and approaches unity in the middle of the bin. The Hanning window used in this work is applied to the bins before the correlations are computed. As the signal rolls off to zero due to the window, the simulated time at these extrema of the bins is 'lost' in the bin itself. Overlapping of the bins ensures this computation time is not lost in the full analysis.

The coherence function can be used to measure the degree of linearity between excitation and response [38]:

$$\gamma^2 = \frac{S_{FX} S_{XF}}{S_{XX} S_{FF}} \tag{3.6}$$

Disturbances (e.g. non-linearities, leakage and noise) result in a non-unity coherence value. When $\gamma^2 << 1$, the FTF is less reliable as the transfer function is a measure of the linear response of the flame to an excitation.

3.1.2 Impulse excitation

Impulse excitation imposes a perturbation pulse to the inlet. The system is simulated in time until a quasi-steady state is reached. An impulse is applied (3% of the mean value) and the system is simulated until it returns to the quasi-steady state. The minimum pulse length is the time step Δt used in the simulation. In this work, the pulse width is set to $10\Delta t$ to ensure the pulse is not lost in noise. For a detailed explanation of the impulse excitation method, the reader is referred to Polifke [34].

The system is simulated in time and the HRR is sampled. The FTF H_f for impulse excitation can be found using:

$$H_f(\omega) = \sum_{k=1}^{m} \frac{Q'(\tau_k)}{\phi'} e^{-i\omega\tau_k} \tag{3.7}$$

Here, m is the total number of time steps before the system returns to the quasi-steady state, $\dot{Q}'(\tau_k) = \dot{Q}(\tau_k) - \overline{\dot{Q}}$ is the volume integrated HRR at time τ_k, and ω is the frequency.

Impulse excitation has a shorter simulation time compared to white noise excitation, as only a single pulse is applied and damped in time. The simulation can be stopped when the system has settled. This method does require an initial simulation time before a pulse is applied, as the pulse can be lost otherwise. White noise does not require this as the hanning window applied to the first bin covers this effect and an averaging procedure is applied. A disadvantage of impulse excitation is that the excitation level is not equal for all frequencies. The quality of the pulse is low and contains a high crest factor. This can excite non-linearities in the system which can lead to undesirable side effects in the FTF computation.

3.2 LINEAR COEFFICIENTS METHOD

In the previous sections, transient based methods have been discussed, which require transient CFD computations to obtain the FTF. A steady state based method is summarized below: the Linear Coefficients Method (LCM). For the full model with numerical and experimental results, the reader is referred to [38].

In CFD analyses, the partial differential equations which are solved can be written as:

$$\frac{\partial \psi_i}{\partial t} = f(\psi_1, \psi_2, ..., \psi_n), \quad i = 1, 2, ..., n \tag{3.8}$$

Here, ψ_i are the independent variables at a node and n is the total number of variables. Steady state values are obtained when $f = 0$. The basis of the LCM is perturbing the independent variables $\boldsymbol{\psi}$ in this steady state solution and determining the change in $\frac{\partial \psi_i}{\partial t}$. Small perturbations are applied to the solution, such that $\psi = \overline{\psi} + \psi'$. Linearizing the partial differential equations around the mean value (and neglecting higher order terms) results in:

$$\frac{d\psi_i'}{dt} = \sum_{j=1}^{n} a_{ij}\psi_j', \quad i = 1, 2, ..., n \tag{3.9}$$

where coefficients a_{ij} represent the linear relation between ψ_j' and the rate of change of ψ_i'. These coefficients can be combined in a coefficient matrix $\boldsymbol{A}$, where

$$\frac{d\boldsymbol{\Psi}'}{dt} = \boldsymbol{A}\boldsymbol{\Psi}' \tag{3.10}$$

The $\boldsymbol{A}$-matrix contains the linear (relation) coefficients and $\boldsymbol{\Psi}'$ is the vector of perturbed independent variables.

To find the response to a varying inlet condition, these perturbations should be included in the unsteady equations, where (it is assumed) only one inlet variable is perturbed (e.g. equivalence ratio ϕ):

$$\frac{d\boldsymbol{\Psi}'}{dt} = \boldsymbol{A}\boldsymbol{\Psi}' + \boldsymbol{B}\phi' \tag{3.11}$$

Here, $\boldsymbol{B}$ is a vector containing the linear relation between ϕ' and $\frac{d\boldsymbol{\Psi}'}{dt}$.

As in Section 3.1, the FTF will consider the HRR response to an equivalence ratio perturbation. As such, the (volume integrated) unsteady HRR response Q' needs to be obtained. Q' is a function of the Ψ' and ϕ'. Linearizing results in:

$$Q' = \boldsymbol{C}\boldsymbol{\Psi}' + D\phi' \tag{3.12}$$

Equations 3.11 and 3.12 are combined in a single state space formulation (single input, single output) The transfer function H_f at a frequency ω can be found from these matrices as:

$$H_f(\omega) = \frac{Q'}{\phi'} = \boldsymbol{C}(i\omega\boldsymbol{I} - \boldsymbol{A})^{-1}\boldsymbol{B} + D \tag{3.13}$$

Here $\boldsymbol{I}$ is the identity matrix.

In the LCM, the FTF does not contain a truncation error in time and does not require transient CFD computations. Determining the inverse of $i\omega\boldsymbol{I} - \boldsymbol{A}$ is impractical in CFD applications, so an order reduction is required. The current LCM implementation in Matlab uses the implicitly restarted and shifted Lanczos method. The full system is approximated by a reduced order system, which in turn is substituted in Equation 3.13 to find the approximated FTF. Limitations of the LCM include apparent sensitivity to the level of excitation and the first-order upwind scheme used for the spatial discretization, which introduces artificial dissipation to the system.

Chapter 4

Methodology

In this chapter, the methods of determining the answers to the research questions are explained. Section 4.1 discusses the basic setup of the CFD computation to obtain the steady state solution of the combustion chamber. A more detailed description of the CFD model can be found in Appendix A. Section 4.1.1 and 4.1.2 compare two combustion models, Finite Rate/Eddy Dissipation model and the UT-Flamelet Genereted Manifold, for use in this work. The setup of the transient computations and LCM computation is discussed in Sections 4.2 and 4.3, respectively. Section 4.4 explains the setup of the ANM.

4.1 COMPUTATIONAL FLUID DYNAMICS MODELING APPROACH

To obtain the FTF using the different methods, a good steady state solution of the combustion must be obtained. A species distribution (or equivalently a mixture fraction distribution) at the combustion chamber inlet is required for the final steady state and transient simulations. To obtain this distribution, the species transport is modeled using Ansys CFX's built-in species transport from the Hydrogen Air library data. These transport equations consider the non-unity Lewis number of separate species. The $k-\omega$ Shear Stress Transport (SST) turbulence model is used for the turbulence. This model was chosen based on expert CFD experience.

The condensing boiler is simulated from the air and hydrogen inlets to the heat exchanger. The CFD simulations use subdomains of the full geometry to increase mesh refinement. Appendix A contains more information on the steps taken to obtain a mesh independent result for the flow in the combustion chamber. The geometry of the burner wall is too complex to resolve with a grid due to the numerous perforations. Consequently, a porous zone is used to approximate the effect of these perforations. Appendix B covers the modeling parameters for the porous medium used in the CFD simulations.

4.1.1 Combustion model

Ansys CFX solves the following species transport equation for each species, i, in the flow [3]:

$$\frac{\partial(\overline{\rho}\widetilde{Y}_i)}{\partial t}+\frac{\partial(\overline{\rho}\widetilde{u}_j\widetilde{Y}_i)}{\partial x_j}=\frac{\partial}{\partial x_j}\left(\Gamma_{i_{eff}}\frac{\partial\widetilde{Y}_i}{\partial x_j}\right)+S_i \tag{4.1}$$

Here, Y_i is the mass fraction of species i, $\Gamma_{i_{eff}}$ is the effective molecular diffusion coefficient[1] and S_i is a chemical source term. The tilde over the variables indicates Favre averaged variables. For reaction k in the flow, the chemical equilibrium can be written as

$$\sum_{i=1}^{n_c} \nu'_{ki}\chi_i \Leftrightarrow \sum_{i=1}^{n_c} \nu''_{ki}\chi_i \tag{4.2}$$

where n_c is the number of components in the flow, i is the chemical symbol of the species and ν'_{ki} and ν''_{ki} are the forward and backward stoichiometric coefficients, respectively. The chemical source term is computed by

$$S_i = W_i \sum_{k=1}^{K} \left(\nu''_{ki} - \nu'_{ki}\right) R_k \tag{4.3}$$

Here, W_i is the species molecular weight and R_k is the reaction rate. To obtain the reaction rate, a combustion model is required. Different options are available for the combustion model, with differences in validity and performance. Below, a selection of combustion models relevant for this study is explained.

Finite rate chemistry

Finite rate chemistry is based on the idea that chemical reactions occur at a limited rate governed by reactant concentration and temperature [3]. The reaction rate, R_k, is determined using a forward reaction rate coefficient, F_k, which has an Arrhenius-like temperature dependence:

$$F_k = A_k T^{\beta_k} \exp\left(-\frac{E_k}{RT}\right) \tag{4.4}$$

Here, A_k, β_k and E_k are reaction rate parameters for reaction k, R is the universal gas constant, T is the temperature. This forward rate coefficient scales the reaction rate determined by the products of the species concentrations in the reaction, as

$$R_{k,FR} = F_k \prod_{i=1}^{n_c} [X_i]^{r'_{ki}} \tag{4.5}$$

where $[X_i]$ is the concentration of species i (see Equation 4.2) and r'_{ki} is a rate exponent for reactant i (in reaction k). This reaction rate can be extended to model reversible reactions:

$$R_{k,FR} = F_k \prod_{i=1}^{n_c} [X_i]^{r'_{ki}} - B_k \prod_{i=1}^{n_c} [X_i]^{r''_{ki}} \tag{4.6}$$

Here, B_k is the backward reaction rate coefficient and r''_{ki} is the rate exponent for product i (in reaction k).

[1] $\Gamma_{i_{eff}}$ is a modified version of Γ_i that models turbulent scalar fluxes, such as mass fractions, using the eddy dissipation assumption [3] as

$$-\overline{\rho Y_i'' \boldsymbol{u}_j''} = \frac{\mu_t}{Sc_t}\frac{\partial \widetilde{Y}_i}{\partial x_j}$$

where μ_t and Sc_t are the turbulent viscosity and turbulent Schmidt number, respectively.The effective molecular diffusion coefficient then becomes

$$\Gamma_{i_{eff}} = \Gamma_i + \frac{\mu_t}{Sc_t}$$

Finite rate chemistry uses the species concentrations to compute the reaction rate. The model works well for slow chemistry and small turbulence-chemistry interaction [2]. The slow chemistry can be characterized by the Damköhler number, a non-dimensional ratio of flow time scale, τ_t, to chemical time scale, τ_c. In turbulent combustion, the Damköhler number is defined using the turbulent mixing time scale:

$$Da = \frac{\tau_t}{\tau_c} \tag{4.7}$$

When $Da << 1$, the turbulent mixing time scales are smaller than the (comparatively slow) chemical time scale. Finite rate chemistry is suitable for low Damköhler numbers.

Eddy dissipation model

A different combustion model that works well for high Damköhler numbers is the Eddy Dissipation Model (EDM). When the chemical kinetics are faster than the turbulent time scales, mixing of the reactants is the limiting factor. The EDM assumes products are produced spontaneously when the species mix on a molecular level. The reaction is limited by this mixing time scale as:

$$R_{k,EDM} = A\frac{\varepsilon}{k}\min\left(\frac{[X_i]}{\nu'_{ki}}\right) \tag{4.8}$$

Here, A is a rate coefficient, k and ε are the turbulence kinetic energy and turbulent eddy dissipation, respectively, for the $k-\varepsilon$ turbulence model, and ν'_{ki} is the stoichiometric coefficient of species i (in reaction k). Compared to finite rate, EDM is cheaper to solve but generally less accurate as temperature dependence is not considered.

Finite rate / Eddy dissipation model

These two combustion models can be combined to for the Finite Rate/Eddy Dissipation Model (FR/EDM). FR/EDM compares the two separate combustion models and uses the lowest reaction rate. This method essentially slows the reaction rate relative to the two separate models, but allows it to function in a wide range of Damköhler numbers. The same scalar advection-diffusion equation (Equation 4.1) is solved, although it is computationally more expensive to determine S_i.

Flamelet Generated Manifold

The Flamelet Generated Manifold (FGM) [12, 30, 39] combustion model differs from FR/EDM in how the reaction rate is determined. FR/EDM transports the individual species and computes the reaction rate in each control volume based on these species concentrations. FGM is based on tabulated chemistry where the chemical kinetics are precomputed from One-Dimensional (1D) premixed flames and interpolation between these predetermined values is used to find the chemical source term. The FGM method considers a multi-dimensional flame (as analyzed in this work) as a set of 1D flames.

The freely propagating 'steady, laminar, adiabatic, unstretched flamelets' [13] are solved using a 1D flame solver (e.g. Chemkin II PREMIX [19]). The GRI-Mech 3.0 is used in the description of the chemistry for UT-FGM. The flamelets are transformed to a reaction progress space, where

the flame is described by a reduced set of control variables. The control variable for a laminar, premixed flame is the scaled Reaction Progress Variable (RPV) c. The unscaled RPV η,

$$\eta = \sum_{k=1}^{K} b_k Y_k \tag{4.9}$$

is the weighted sum of the mass fractions k of all species K. The weights b_k are chosen based on the Computational Singular Perturbation algorithm which removes the fast chemical time scales, resulting in a more uniform scaled RPV [12]. c is scaled such that $c = 0$ is the unburnt state and $c = 1$ is the burnt state of the mixture, using:

$$c = \frac{\eta - \eta^u}{\eta^b - \eta^u} \tag{4.10}$$

Here, η^b and η^u are the unscaled RPVs for the burnt and unburnt state, respectively. The chemical source term S_c is obtained similarly as

$$S_c = \frac{\sum_{k=1}^{K} b_k \dot{\omega}_k}{\eta^b - \eta^u} \tag{4.11}$$

Here, $\dot{\omega}_k$ is the mass production rate of species k. Note, the FGM model only uses one chemical source term, where FR/EDM computes a source term for every species in the flow.

In non-premixed and partially premixed combustion, the ratio of fuel to oxidizer mass fraction is not constant in the domain. Consequently, a second control variable is defined to transport species: the mixture fraction f, calculateed using Bilger's definition [40]. $f = 0$ for a pure oxidizer and $f = 1$ for a pure fuel.

Turbulent, partially premixed flames are considered in this work, requiring two additional control variables: $c_v \equiv c''^2$ and $f_v \equiv f''^2$ for the variance in (scaled) RPV and mixture fraction, respectively. Following from the definition, these variances cover the non-linear fluctuating term in the turbulent transport of these variables. A presumed β-Probability Density Function (PDF) is applied for the (scaled) RPV and the mixture fraction [12]. When the variance goes to zero, the shape of the β-PDF approaches a δ-PDF. The PDF is used in the Favre-averaging of the RPV and mixture fraction.

The following (Favre-averaged) transport equations are solved in the FGM model for the mean RPV, mean mixture fraction, RPV variance and mixture fraction variance, respectively:

$$\frac{\partial(\overline{\rho}\widetilde{c})}{\partial t} + \nabla \cdot (\overline{\rho}\widetilde{\boldsymbol{u}}\widetilde{c}) = \nabla \cdot [(\overline{\rho}\overline{D} + \overline{D}_t)\nabla\widetilde{c}] + \widetilde{S}_c \tag{4.12}$$

$$\frac{\partial(\overline{\rho}\widetilde{f})}{\partial t} + \nabla \cdot (\overline{\rho}\widetilde{\boldsymbol{u}}\widetilde{f}) = \nabla \cdot [(\overline{\rho}\overline{D} + \overline{D}_t)\nabla\widetilde{f}] \tag{4.13}$$

$$\frac{\partial(\overline{\rho}\widetilde{c}_v)}{\partial t} + \nabla \cdot (\overline{\rho}\widetilde{\boldsymbol{u}}\widetilde{c}_v) = \nabla \cdot [(\overline{\rho}\overline{D} + \overline{D}_t)\nabla\widetilde{c}_v] + 2(\widetilde{S_c c} - \widetilde{S_c}\widetilde{c}) + \overline{P}_{k_c} + \overline{D}_{k_c} \tag{4.14}$$

$$\frac{\partial(\overline{\rho}\widetilde{f}_v)}{\partial t} + \nabla \cdot (\overline{\rho}\widetilde{\boldsymbol{u}}\widetilde{f}_v) = \nabla \cdot [(\overline{\rho}\overline{D} + \overline{D}_t)\nabla\widetilde{f}_v] + \overline{P}_{k_f} + \overline{D}_{k_f} \tag{4.15}$$

Here, ρ is the density, $\boldsymbol{u}$ the velocity, D the laminar diffusivity and D_t the turbulent diffusivity.

The production and dissipation terms, $\overline{P}_{k_c}$, $\overline{D}_{k_c}$, $\overline{P}_{k_f}$ and $\overline{D}_{k_f}$, are defined as:

$$\overline{P}_{k_c} = 2\frac{\mu_t}{Sc_t}|\nabla\widetilde{c}|^2 \tag{4.16}$$

$$\overline{D}_{k_c} = -2\overline{\rho}\frac{\varepsilon}{k}\widetilde{c}_v \tag{4.17}$$

$$\overline{P}_{k_f} = 2\frac{\mu_t}{Sc_t}|\nabla\widetilde{f}|^2 \tag{4.18}$$

$$\overline{D}_{k_f} = -2\overline{\rho}\frac{\varepsilon}{k}\widetilde{f}_v \tag{4.19}$$

$\overline{D}$ is determined based on the unity Lewis assumption. The (mixture averaged) Lewis number is a non-dimensional ratio of thermal diffusivity to mass diffusivity:

$$Le = \frac{\alpha}{D} = \frac{\lambda}{\rho c_p D} \tag{4.20}$$

Here, α is the thermal diffusivity, D the mass diffusivity, λ the thermal conductivity, ρ the density and c_p the specific heat capacity at constant pressure. The Lewis number can be chosen to equal unity to simplify the governing equations.[2] These equations become more complex when each species in the flow has a non-unity Lewis number, as in [28]. For hydrogen in air, the Lewis number is less than unity, meaning mass diffusion is preferred. This influences combustion characteristics [22], such as flame shape and location of heat release rate. This aspect of preferential diffusion is not considered in the used FGM implementation.

4.1.2 Comparison of combustion models

In this work, the FR/EDM and FGM model are compared on the combustion in the hydrogen burning system. The flames will be compared based on the flame length, temperature distribution and combustion regimes.

Flame length

Figure 4.1 shows the shape of the flame differs between the two combustion models used. In Figure 4.1(a), a comparison is shown of the normalized temperature distribution. The dark blue is the minimum temperature at the combustion chamber inlet ($T = T_{inlet}$) and the yellow region indicates temperature values near the global maxima. The FR/EDM simulation has a significantly longer and wider shape than the FGM result. The FGM flame also shows a steeper gradient along the entire flame front (also at the root of the flame). A similar result is seen when comparing the normalized hydrogen content in the flow. The flame is wider and longer for FR/EDM and FGM shows a steeper gradient.

The flame thickness can be computed separately for a flame with an equivalence ratio identical to the simulated case ($\phi = \phi_{design}$). Using Cantera [9], a 1D free flame is simulated with the mean flow parameters used for the result above. A multi-component transport model is used to consider the effects of preferential diffusion of hydrogen[3]. A flame thickness can be computed from this

[2] This is done in the UT-FGM model implementation in Ansys CFX.

[3] When the free flame is simulated with the unity Lewis number transport model, the flame (thermal) thickness reduces by 15%, showing preferential diffusion plays a role in thickening a flame.

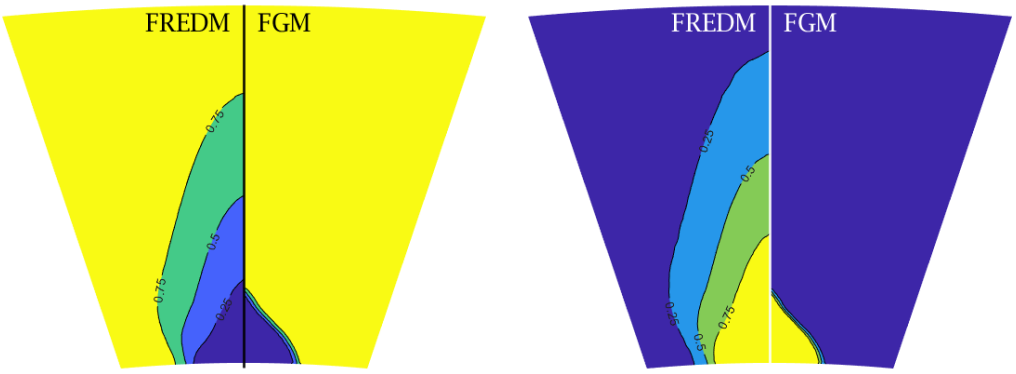

(a) Normalized temperature distribution.

(b) Normalized hydrogen content.

Figure 4.1: Qualitative comparison of the flame shape for the two combustion models. The radial cross section is taken at a reference point in the flame. The temperature is normalized by the adiabatic flame temperature at the design equivalence ratio. The hydrogen content is the mass fraction scaled between 0 and 1.

simulation by considering the 'thermal thickness,' δ_L^0 [32]:

$$\delta_L^0 = \frac{T_2 - T_1}{\max\left(\left|\frac{\partial T}{\partial x}\right|\right)} \tag{4.21}$$

Here, this thickness is computed from the temperature jump across the flame ($T_2 - T_1$) divided by the maximum gradient ($\max\left(\left|\frac{\partial T}{\partial x}\right|\right)$). The thickness for the flame for $\phi = \phi_{design}$ is $\delta_L^0 \sim 10^{-4}$m.This is comparable to the flame thickness according to the FGM model. The FR/EDM results in a flame thickness 2 orders of magnitude higher compared to the result from Cantera.

Temperature

The temperatures in the domains can be compared quantitatively to the adiabatic flame temperature result from Cantera. In Cantera, the adiabatic flame temperature can be found using the `equilibrate('HP')` function. This function uses the built-in chemical equilibrium solver [10], keeping the specific enthalpy (`H`) and pressure (`P`) constant in the chemical equilibrium. The normalized mean and maximum temperature after combustion are shown in Table 4.1.

Table 4.1 Flame temperatures in the domain for different combustion models. Values in Cantera are computed from the reference values used in the simulations. ϕ_{design} is the design specification of the condensing boiler; ϕ_{max} is the highest equivalence ratio at the inlet. The temperatures are normalized by the adiabatic flame temperature at ϕ_{design}.

	$\overline{T}_{\text{mean}}$	$\overline{T}_{\text{max}}$
FR/EDM	0.985	1.137
FGM	0.979	1.095
Cantera ($\phi = \phi_{design}$)	1	-
Cantera ($\phi = \phi_{\text{max}}$)	-	1.094

The mean temperatures are differ between FR/EDM, FGM and the result from Cantera. A possible reason for this difference from the Cantera computation might be due to the non-uniform equivalence ratio distribution along the burner surface. Some parts of the combustion chamber inlet approach an equivalence ratio of $\phi = 1$, whereas other parts are far leaner than the design equivalence ratio. At lower equivalence ratios, the adiabatic flame temperature drops significantly (see Figure 4.2). The gradient of this curve decreases for increasing equivalence ratio, meaning a difference in ϕ in a lean flame has more effect on the temperature than a flame operating near stoichiometric conditions. This can reduce the mean temperature in the combustion chamber.

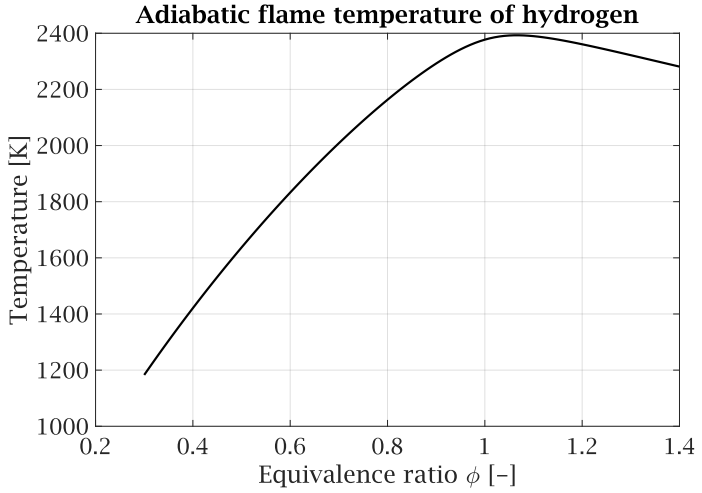

Figure 4.2: Adiabatic flame temperature as a function of equivalence ratio for hydrogen. Values are computed in Cantera from normal temperature and pressure (20°C; 1 atm) [17].

The maximum temperature in the domain for FGM is nearly identical to the flame computed using Cantera. The flamelets used for the UT-FGM model are computed using Cantera, which may be the reason for the agreement between the two computations. FR/EDM overestimates the maximum temperature by $0.043T_{ref}$, exceeding the maximum adiabatic flame temperature of hydrogen (given the normal temperature as reference). The cause of this might be the high flame thickness. As the reaction occurs, temperatures increase in the flow. This, combined with the preferential diffusion effect considered in the FR/EDM transport equations, can produce higher equivalence ratio sections for an effectively preheated flow. As such, the adiabatic flame temperature computed from normal temperature can be exceeded.

If the flame thickness is the reason for the high maximum temperature in the FR/EDM result, then the FGM result is more accurate. Above, the expected flame thickness was shown to be exceeded by two orders of magnitude for the FR/EDM result, whereas FGM was in good agreement with this result. The agreement between FGM and Cantera for the maximum temperature shows the correct implementation in CFX of the UT-FGM model.

Combustion regime

Another way of determining the validity of a combustion model is based on the combustion regime. In turbulent premixed combustion, flames can be characterized by two non-dimensional

numbers: The Damköhler number and the Karlovitz number. From before, the Damköhler number is the ratio of the turbulent mixing timescale to the chemical time scale (Equation 4.7). For the $k - \varepsilon$ turbulence model, this number is computed as:

$$Da = \frac{k}{\varepsilon} \frac{s_L^0}{\delta_L^0} \tag{4.22}$$

Here, the k is the turbulent kinetic energy; ε is the turbulent eddy dissipation; s_L^0 is the laminar flame speed; and δ_L^0 is the flame thickness estimate. The first fraction represents the turbulent time scale, τ_t. The second fraction represents the inverse of the chemical time scale, τ_c. High Damköhler numbers represent fast chemistry, where macro mixing is leading in the combustion. A small Damköhler number represents a combustion process where the mixture is mixing rapidly (on large length scales) and the chemistry is slow.

In the flow, a smallest length scale can be defined: the Kolmogorov scale. Micro mixing of species takes place at these scales. The Kolmogorov length scale, η, and velocity scale u_η are:

$$\eta = \nu^{\frac{3}{4}} \varepsilon^{-\frac{1}{4}} \tag{4.23}$$

$$u_\eta = \nu^{\frac{1}{4}} \varepsilon^{\frac{1}{4}} \tag{4.24}$$

Using these definitions, a micro mixing time scale can be defined as η / u_η. This micro mixing time scale is combined with the chemical time scale in the Karlovitz number, Ka:

$$Ka = \sqrt{\frac{\varepsilon}{\nu}} \frac{\delta_L}{s_L^0} \tag{4.25}$$

The Karlovitz number is the ratio of chemical time scale to turbulent micro mixing time scale. A high Karlovitz number therefore represents good micro mixing, where the chemical time scales are leading in the process.

As such, the Damköhler and Karlovitz numbers combined can describe a flame based on chemical time scales, macro and micro mixing. These non-dimensional numbers are related to each other with the macro scale turbulent Reynolds number, Re_t. It can be shown that $Re = \frac{k^2}{\nu\varepsilon}$ by taking the characteristic velocity scale as a velocity fluctuation $u' = \sqrt{k}$ and the characteristic length scale as $L = \frac{k^{3/2}}{\varepsilon}$ As the turbulent kinematic viscosity, ν_t, for the $k - \varepsilon$ turbulence model is defined as

$$\nu_t = C_\mu \frac{k^2}{\varepsilon} \tag{4.26}$$

the macro mixing turbulent Reynolds number can be written as the ratio of the turbulent kinematic viscosity to the (laminar) kinematic viscosity:

$$Re_t = \frac{\nu_t}{\nu} = Da^2 Ka^2 \tag{4.27}$$

When the turbulent Reynolds number is unity, the eddy viscosity and the kinematic viscosity are equal. For lower values, the laminar viscosity is greater than the turbulent viscosity. In a combustion process, this would lead to laminar combustion. For values of $Re_t > 1$, the approximate values of Damköhler and Karlovitz compared to unity become important.

For both combustion models, the Damköhler and Karlovitz numbers in the flame can be computed and plotted in a figure (see Figure 4.3 and 4.4 for FR/EDM and FGM, respectively). In these figures, the line of $Re_t = 1$ is shown in black, separating turbulent combustion processes from laminar combustion. Three other regions are identified:

- Flamelets: When $Da >> 1$ and $Ka << 1$, the chemical time scale is smaller than both macro and micro mixing scales. The chemistry occurs in thin layers (flamelets) in the turbulent flow field [31]. On this layer (in pre-mixed combustion), the flame acts one-dimensional and propagates from the burnt mixture to the unburnt mixture with the flame speed. Combustion occurs at length scales smaller than the Kolmogorov scale. In other words, the flame is thinner than all turbulent scales [32].
- Thickened flames: The thickened flame regime, also referred to as the distributed reaction regime, has slow macro mixing and fast micro mixing compared to the chemical reaction rate. As such, on the macro scale mixing is leading, while on the micro scale the reaction rate is leading. The flame is thicker than the micro mixing scale, leading to the name 'thickened flame.'
- Well stirred reactor: For $Da << 1$ and $Ka >> 1$, the turbulent mixing is faster than the reaction time scale. These combustion processes are reaction rate dominated

For the FR/EDM-result, the values for Damköhler and Karlovitz are computed in the region of the flame using Equation 4.22 and 4.25, respectively. The region is selected where the mass fraction of hydrogen, Y_{H_2}, is larger than a threshold value: $Y_{H_2} \geq 10^{-4}$. The result did not change significantly when changing this threshold value. It can be seen most points are located in the flamelets region. Some points are in the laminar combustion regime ($Re_t < 1$).

As such, a model that is valid in the flamelet region should be applied, according to this result. The finite rate combustion model is valid for laminar flames; the eddy dissipation model is valid for high turbulence. The set of points at the top right lies on the line $Re_t \approx 45$. As such, the points in the figure all have a turbulent Reynolds number less than 45. This implies the points are weakly turbulent. While FR/EDM might give good results in this region, a combustion model designed for flamelets, such as the UT-FGM model, can give more accurate results.

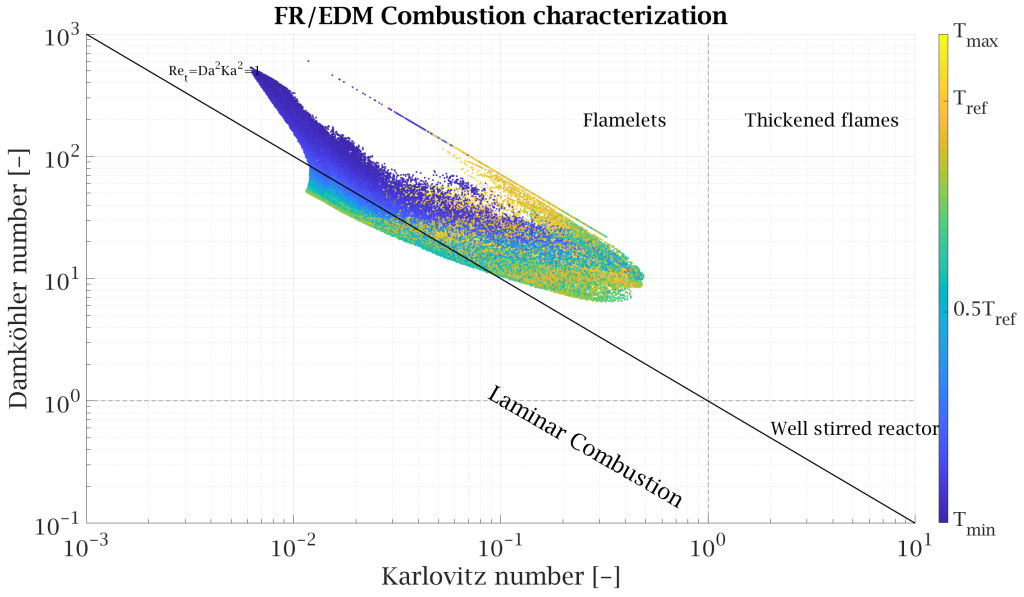

Figure 4.3: Combustion regimes shown for the FR/EDM simulation. Damköhler and Karlovitz numbers are calculated for points where $Y_{H_2} \geq 10^{-4}$ for the flame location. Data points are colored based on the temperature relative to the reference temperature T_{ref}.

When considering the FGM results, the combustion regimes covered by the Damköhler and Karlovitz numbers are slightly different (see Figure 4.4). The points are shifted towards unity Karlovitz and Damköhler, with some points in the thickened flame regime (mostly with $c \approx 0.3$). The FGM model assumes the flame is in the flamelet region, but it is not strictly invalid in the thickened flame region [13]. Resulting from the assumption of isotropic turbulence, which is not accurate at the flame front, the definition of u' is chosen as $u' \approx \sqrt{\frac{2}{3}k}$. The $k-\varepsilon$ model assumes isotropic turbulence in the definition of k. As most of the points in the flame are in the flamelet region, the model is considered valid. Similar to the FR/EDM result, all points in the figure are below the line $Re_t \approx 45$, with a larger portion of the flame in the laminar combustion region. The set of points with $Ka < 10^{-1}$ and $Da > 10$ is mostly comprised of points in the flame where $c < 0.1$.

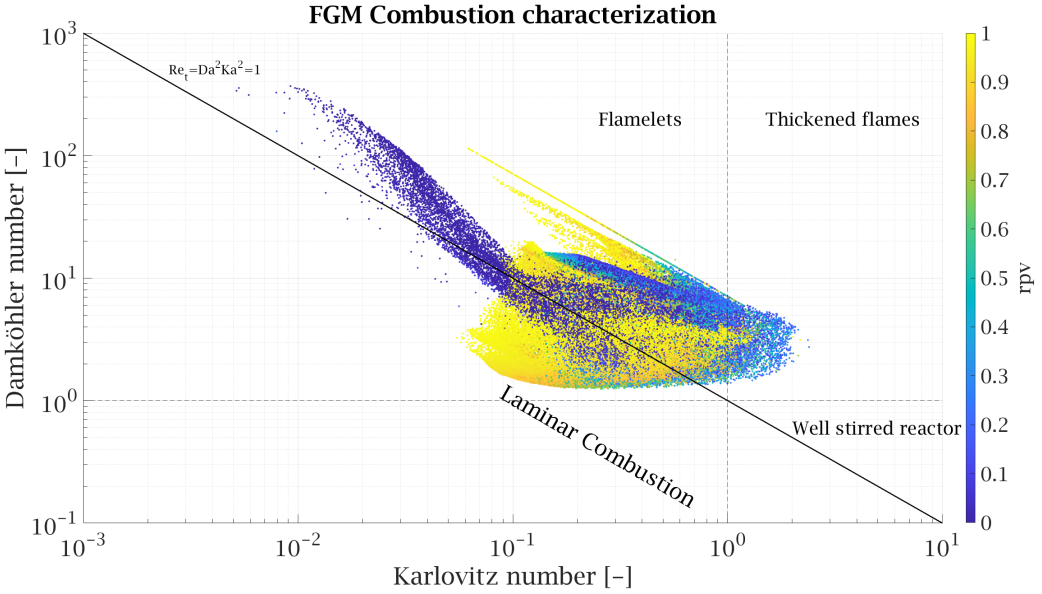

Figure 4.4: Combustion regimes shown for the FGM simulation. Damköhler and Karlovitz numbers are calculated for points where $rpv \leq 0.99$ for the flame location. Data points are colored based on the reaction progress variable.

Concluding remarks

The three metrics above can be used to determine which combustion model can be used. When considering the flame length and flame thickness, the V-shaped flame from FGM is more inline with expected values from 1D-equations. The flame front for FR/EDM is two orders of magnitude thicker than the FGM result. In addition, the FGM-model does not overestimate the maximum temperature in the domain. While both models are generally in the valid combustion regimes, a flamelet based model is likely more accurate than FR/EDM. The choice is made to continue with the FGM-model as the flame produced in these simulations seems to reflect the real situation more accurately, although emperical results are not present to verify this.

4.2 TRANSIENT BASED METHODS

For the transient computations, a time step and total duration need to be determined. Similar to the work by [38], the time step is determined by considering the characteristic frequencies in the flow field near the flame. This characteristic frequency is determined by computing the turbulent frequency field using

$$f_{turb} = \frac{\varepsilon}{k} \tag{4.28}$$

While this is a good indication of the characteristic frequency, the value is an overestimate. The inverse gives the time scale to dissipate all turbulent energy (given local conditions). Using the non-dimensional quantities from Section 1.4, the characteristic Strouhal numbers found by non-dimensionalization of Equation 4.28 is $St_{turb} = 0.72$. Taking 40 time steps per period for a low error in time results in the time step:

$$\Delta\bar{t} = \frac{1}{St_{turb}}\frac{1}{40} = \frac{1}{0.72}\frac{1}{40} = 0.018 \tag{4.29}$$

Higher frequency behaviour is expected to be dominant, considering the effect of hydrogen on the intrinsic thermoacoustic modes [7]. With hydrogen as a fuel source, thermoacoustic modes shift to higher Strouhal numbers.

The mesh independent result of the FGM simulation (using flame front elements with $\Delta\overline{x} = 0.368$) is used as the initial condition for the transient runs. The solution is simulated in time until the volume integrated heat release has settled into steady behaviour before the excitation is applied. For the impulse simulation, the equivalence ratio is excited for 10 time steps to ensure a strong enough effect. The volume integrated heat release is sampled at every time step starting from the excitation.

For the white noise simulation, the new excitation is held for 10 time steps each time before switching to the new time step. This choice is made to ensure a significant signal-to-noise ratio. Consequently, the sampling frequency for the white noise simulation is reduced by a factor 10, to only sample at the start of the new excitation[4]. This reduces the sampling frequency computed before (by taking the inverse of Equation 4.29) by a factor 10 as well. The resulting highest frequency to be considered for the FTF is the Nyquist frequency, $f_N = f_s/2$. The Strouhal number corresponding to this frequency is $St_{max} = 2.79$ The white noise simulation has a total duration of $\bar{t} = 717$, to allow for averaging of multiple overlapping samples in the result. This is done to suppress the effect of non-linearities. The white noise is generated using Matlab's `rand( )`-function. This function generates uniformly distributed pseudorandom numbers.

4.3 LINEAR COEFFICIENT METHOD

To obtain the results using the LCM, the same steady state simulation is used as for the transient simulations. Flow field data is exported from the CFD result to Matlab. The FGM implementation requires a database to be loaded in. The flamelet database used here is a unity Lewis turbulent

[4]It is found that there is no significant difference in amplitude or phase in the result if every time step is sampled, other than additional peaks at integer multiple Strouhal values of $St_{max} = 2.79$. These are a result of the choice to keep the impulse high for 10 time steps. 5 of these peaks are seen up to and including the Nyquist frequency.

database. The UT-FGM implementation in Ansys CFX does not allow differential diffusion for the combusting flow. As such, the unity Lewis assumption is used for all FGM results in this work.

An equivalence ratio perturbation is used as the fluctuating inlet variable to compute the $\boldsymbol{B}$ and $\boldsymbol{D}$ matrices, similar to the transient simulations. The amplitude of this perturbation is set to 1%. For computing the coefficient matrix $\boldsymbol{A}$, independent variables ψ are selected to be perturbed. The variables selected are velocity (three directions), enthalpy, reaction progress variable and mixture fraction. The enthalpy variable is selected, as enthalpy is transported in the simulation (adiabatic walls are still used). The enthalpy values used in constructing the $\boldsymbol{A}$-matrix are taken from the simulation, rather than interpolated using the mixture fraction Z. This linear fit between the enthalpy at $Z = 0$ and $Z = 1$ is not a perfect fit for all values in the simulation.

The LCM code allows the user to filter the nodes, based on their relevance to the flame. Nodes very far away from the flame do not influence the matrices and, consequently, the FTF. A new filter is introduced to select based on radial distance from the global Y-axis, as the geometry has a cylindrical shape. Only nodes within a relevant radius are considered in the construction of the $\boldsymbol{A}$ and $\boldsymbol{C}$-matrices. Due to the positioning of the inlets to the combustion chamber, some areas in this volume do not contribute to the calculation. An extra filter based on the Heat Release Rate (HRR) is applied. Only nodes with a HRR above a (low) threshold value are considered. These filters reduce the number of points in the computation by 28%. The resulting $\boldsymbol{A}$-matrix is is still large due to the small elements used in the flame region. 342473 control volumes are considered.

The dimension of the state space system is reduced to a low order system using the Lanczos method. This is based on a taylor series expansion around a frequency $s = \sigma$ of transfer function $H(s) = \boldsymbol{C}(s\boldsymbol{I} - \boldsymbol{A})^{-1}\boldsymbol{B}$. Here, $\boldsymbol{I}$ is the identity matrix and $s = i\omega$ is a complex variable in the laplace domain. The normalized value of σ is set to $St = 0.0015$.

The main part of the computation time is in the computations of the coefficients for the $\boldsymbol{A}$ and $\boldsymbol{C}$-matrices. An adaptation to the original code is applied to parallelize the computation of these coefficients, as these calculations are independent. Storing the values in the same matrix after the computation is now the bottleneck of the computation. Without parallelization, calculating the coefficients has a wall clock time in excess of 1 week. With the parallelization implemented, the time reduces with the number of cores used in the 'parallel pool' in Matlab. 32 cores are used in parallel, such that computing the coefficients is in the order of 10 hours. Extrapolating to a single core process, the wall clock time would exceed two weeks. This time requirement is similar to an extensive transient simulation. Note, the coefficient matrices could be obtained from the CFD-solver code, as similar coefficient matrices are generated in the solving process. Ansys CFX 5.6 solves equations sequentially, so the full matrices are not produced at once. An adaptation of the CFX source code would be required to generate these matrices. This would speed up the computation time for LCM significantly.

The parallelization implementation distributes the filtered control volumes over the parallel cores. Each core iterates over the fluctuated variables. As 6 variables are fluctuated, each process runs a similar computation 6 times. The computation time of this step in the LCM code is therefore directly related to the number of evaluated variables. For the FGM implementation in the code, the velocity, rpv and mixture fraction fluctuations are needed for a good result. Enthalpy is added as the sixth variable due to the choice in transporting enthalpy.

The shifted Lanczos method used to reduce the order of the system is performed after the matrices have been obtained. This step does not require the same order of computation time as

the assembly of the large matrices; rather wall clock time is in the order of 5 hours for the 3D CFD simulation compared in this work. Large amounts of memory is required for this computation, however. The reduction method computes the matrix $\boldsymbol{X} = s\boldsymbol{I} - \boldsymbol{A}$. After, it computes the lower-upper triangularisation of the $\boldsymbol{X}$ matrix, generating matrices $\boldsymbol{L}$ and $\boldsymbol{U}$ such that $\boldsymbol{X} = \boldsymbol{LU}$. This step requires large amounts of memory (in excess of 300 GB for the matrices solved in this work), as the $\boldsymbol{L}$ and $\boldsymbol{U}$-matrices are not nearly as sparse as the $\boldsymbol{X}$-matrix. The computational cost of this step is reduced by preconditioning[5] done on the $\boldsymbol{A}$-matrix, which increases the sparsity of the matrix.

4.4 ACOUSTIC NETWORK MODEL

The Acoustic Network Model (ANM) models the entire domain using 1D-elements. These elements need to be chosen such that they reflect the real system. The following system is designed to determine the effect of different FTFs: The relevant boundary conditions and element types

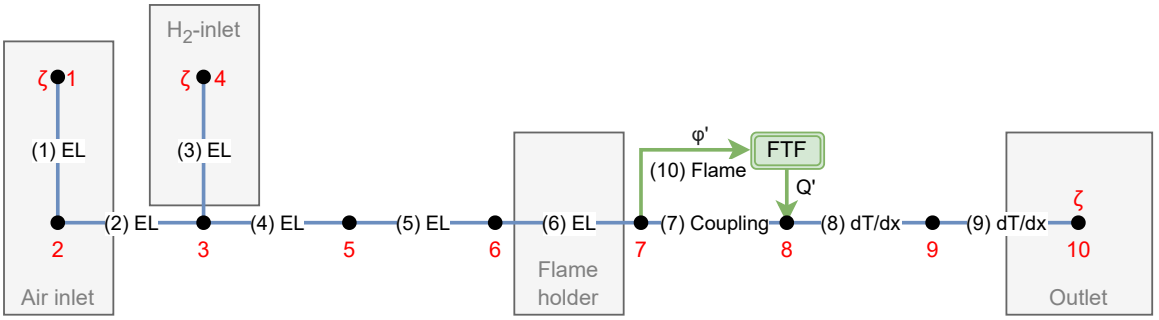

Figure 4.5: Schematic overview of the full acoustic network model used in the comparison of the Flame Transfer Functions (FTF). The nodes (black dots with red index) are connected by 1D elements (blue lines with element number and types). Impedance boundary conditions ζ are applied at the inlet and outlet nodes.

are shown in the figure. For all elements up to the flame, prismatic tubes are used. The rapid expansion from the flame holder to the combustion chamber is modelled as a coupling element. The two elements after are inviscid tubes with a linear axial temperature gradient. A temperature gradient in a system affects the acoustic behaviour. The combustion chamber has the most significant gradients of the entire system.

The mean flow conditions are taken from the CFD simulations. Turbulent damping coefficients, β_t, for the prismatic tubes are calculated using equations from Van Kampen [38], repeated here for completeness:

$$\beta_t = \frac{\psi Ma}{2a} \tag{4.30}$$

Here, Ma is the mean mach number in the tube; a is the ratio of the area of the duct cross-section to the perimeter. The friction factor, ψ, for smooth pipes can be found using Blasius' formula:

$$\psi = 0.3146 Re^{-1/4} \tag{4.31}$$

[5]This preconditioning is performed while the CFD-data and mesh connectivity is read in Matlab. Using 'reverse Cuthill-McKee', the bandwidth of the matrices is reduced by reshuffling the vertices order. See the `readCFXdata()` function.

For the boundary conditions, impedances are prescribed at the air inlet, hydrogen inlet and the combustion chamber exit. Full reflection is assumed at the air and hydrogen inlet resulting from the effect of the fan and geometry constraints, respectively. The sensitivity of the system to the exit impedance is examined (see Section 5.2.1). Additionally, a mass flow perturbation boundary condition is prescribed at the flame (Node 8). The magnitude of this perturbation influences the magnitude of the pressure perturbation. As a linear system $\boldsymbol{Ap'} = \boldsymbol{M'}$ is solved, the frequency behaviour is unaffected by the choice in magnitude of the mass flow perturbation. As such, the perturbation is set to a value related to the heat release rate perturbation seen in the transient simulations. The heat release rate perturbation, q'_f, is converted to an effective mass flow perturbation, m'_s, using [38]:

$$m'_s = \frac{\gamma - 1}{c_0^2} q'_f \tag{4.32}$$

Here, γ is the heat capacity ratio and c_0 is the speed of sound. These parameters are evaluated at the adiabatic flame temperature and assumed to be constant, as it is found this gives a small error.

This fraction is also used to convert the equivalence ratio FTF to a mass flow perturbation FTF. The equivalence ratio perturbation influence on the HRR perturbation is obtained from the simulations. For the ANM, these need to be in the form of a mass flow perturbation per reference mass flow. This conversion is computed using Equation 6.9 in Van Kampen [38], yielding:

$$\frac{M'_Q}{M'_f} \approx H_f \frac{\phi_0}{M_{f,0}} \frac{\gamma - 1}{c_0^2} \tag{4.33}$$

Here, the left hand side is the FTF used in the ANM, H_f is the FTF obtained from simulation, ϕ_0 is the mean equivalence ratio, and $M_{f,0}$ is the mean fuel mass flow rate.

Chapter 5

Results

In this chapter, the results are discussed. First, the FTFs obtained using the different methods are shown. For the impulse excitation simulations (Section 5.1.1), two time steps are compared ($\Delta\bar{t} = 0.018$ and $\Delta\bar{t} = 0.036$). The white noise excitation simulation result (Section 5.1.2) is tuned and compared to the impulse excitation results. Section 5.1.3 discusses the FTF obtained using the LCM. The computation time is compared in Section 5.1.4. The sensitivity study of the ANM is described (Section 5.2) and the different FTFs are compared using the ANM (Section 5.2.4).

5.1 FLAME TRANSFER FUNCTION COMPARISON

For each of the transient methods examined in this work, a flame transfer functions is determined. During transient simulation, it was found the system behaved periodically. This periodic behaviour is analyzed separately under “steady" conditions. The time step for this simulation is set to $\Delta\bar{t} = 0.036$, identical to the second time step used in the impulse excitation run[1]. The percentage difference of the HRR perturbation is shown in Figure 5.1. From this figure, periodic

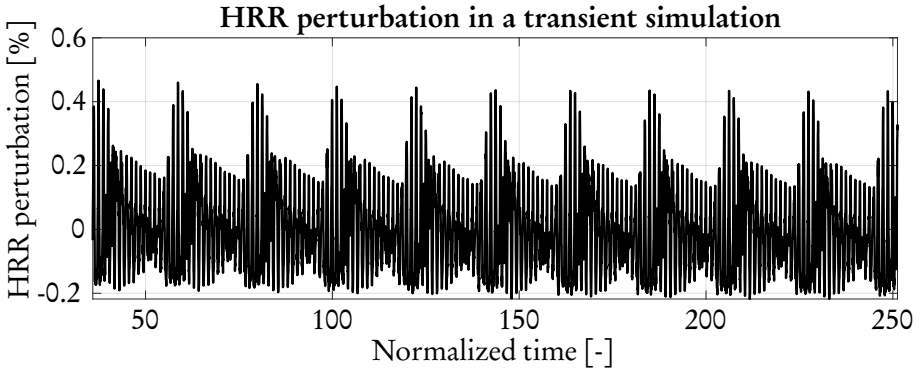

Figure 5.1: Heat release rate perturbation shown as the percentage difference from the mean in a transient simulation of the combustion chamber. The settling time of the simulation is omitted in the graph.

oscillating behaviour becomes apparent. The maximum difference compared to the mean (volume integrated) HRR is 0.46%. This signal can be analyzed using a Fast Fourier Transform (FFT) to find the dominant frequencies making up this signal. This spectral analysis is shown in Figure 5.2.

[1]The impulse excitation simulations showed transient effects which where investigated separately from the impulse simulations. Due to time constraints, a doubled $\Delta\bar{t}$ was chosen.

Three sets of dominant frequencies can be seen, around $St \approx 0.1$, $St \approx 0.75$ and $St \approx 1.5$. The

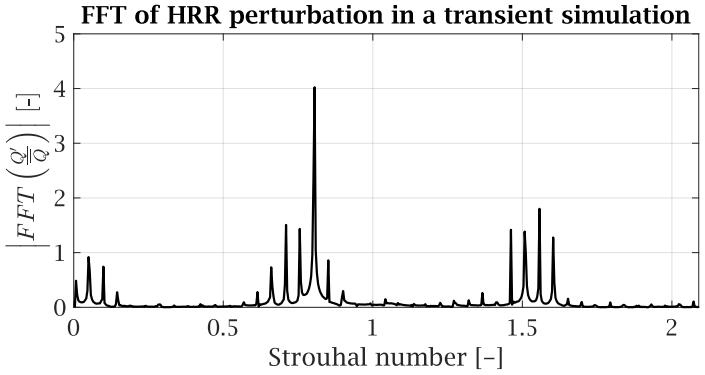

Figure 5.2: Spectral analysis of the heat release rate perturbation. The peaks show dominant frequencies in the signal.

third set appears to be an upper harmonic of the second set. The most dominant frequency is observed at $St = 0.8$ with a first harmonic frequency at $St = 1.6$. The frequencies of the peaks in the FFT act as eigenfrequencies of the system. As such, they can appear in the FTF's generated using the transient methods.

5.1.1 Impulse excitation

Equation 3.7 shows how the FTF is computed from the HRR fluctuations. All time steps m before the response has settled to the unexcited system behaviour are considered in this equation [38]. As such, to determine the FTF, the time behaviour of the HRR fluctuations must be examined. This is done below for two time steps $\Delta\bar{t}$.

Impulse $\Delta\bar{t} = 0.018$

The HRR is plotted in time in Figure 5.3. The HRR initially increases, after which its oscillations dampen out to the periodic behaviour. Superimposed on the figure (and shifted in time) is the HRR of the transient simulation. A time discretization error becomes apparent, where the high frequency behaviour of the transient run lags relative to the impulse excitation result. The low frequency oscillations of the transient run appear to be at a higher frequency than the impulse simulation.

This can be seen in a spectral analysis of the two signals. In Figure 5.4, the results are compared. For the impulse result, the Fourier transformed signal is taken from $\bar{t} = 15$ to the end of the simulation $\bar{t}_{max} = 358$. This shift clearly shows a time discretization error present. For the highest peaks around $St = 0.8$, the difference in Strouhal number is 0.015. For the last peaks shown in Figure 5.4, the difference is 0.045.

The normalized FTF can be computed using the HRR fluctuations before $\bar{t} = 15$. The FTF is shown in Figure 5.6. The reference value for the normalization is chosen to be the first value.

Low-pass behaviour is observed in the gain, where lower frequencies have a high gain and

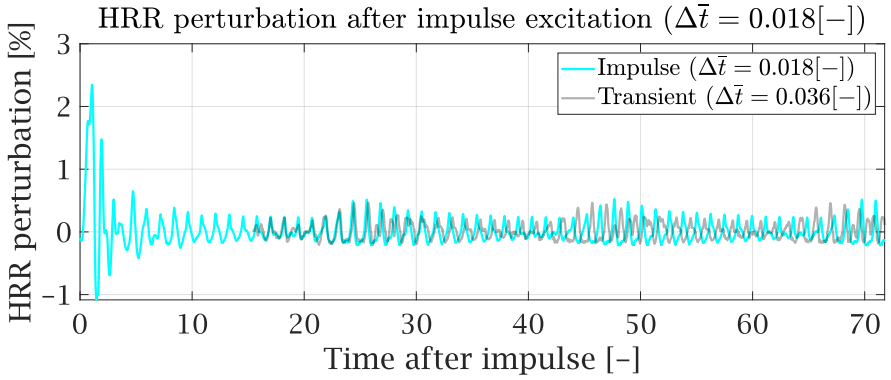

Figure 5.3: Heat release rate fluctuations of the impulse excitation simulation. The time step used in the transient simulation is $\Delta\bar{t} = 0.018$. Periodic behaviour is observed after approximately $\bar{t} = 15$.

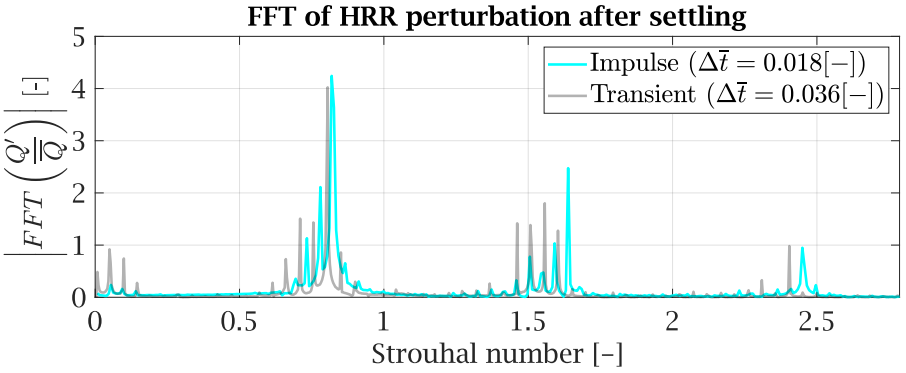

Figure 5.4: Spectral analysis of the heat release rate perturbations of the impulse excitation simulation ($\Delta\bar{t} = 0.018$). The result is compared against the unperturbed transient simulation ($\Delta\bar{t} = 0.036$). A shift in frequency can be observed when comparing the two time steps.

higher frequencies are damped out. Three distinct peaks in the gain can be seen at Strouhal numbers 0.77, 1.04 and 1.67. The peaks at 0.77 and 1.67 seem to correspond to the intrinsic frequencies of the flame, as seen in Figure 5.4. The peak in the FTF at $St = 1.04$ seems unique to the impulse excitation applied. The phase of this point is -2π rad, meaning this oscillation is in phase with an excitation. The peak at $St = 1.67$ has a phase of approximately -4π rad. The 0.77 peak is out of phase, with a phase shift approximately equal to $-\pi$ rad.

Impulse $\Delta\bar{t} = 0.036$

The impulse excitation simulation is repeated for a doubled $\Delta\bar{t}$ to examine the effect of a time discretization error. The HRR is plotted in time in Figure 5.5.

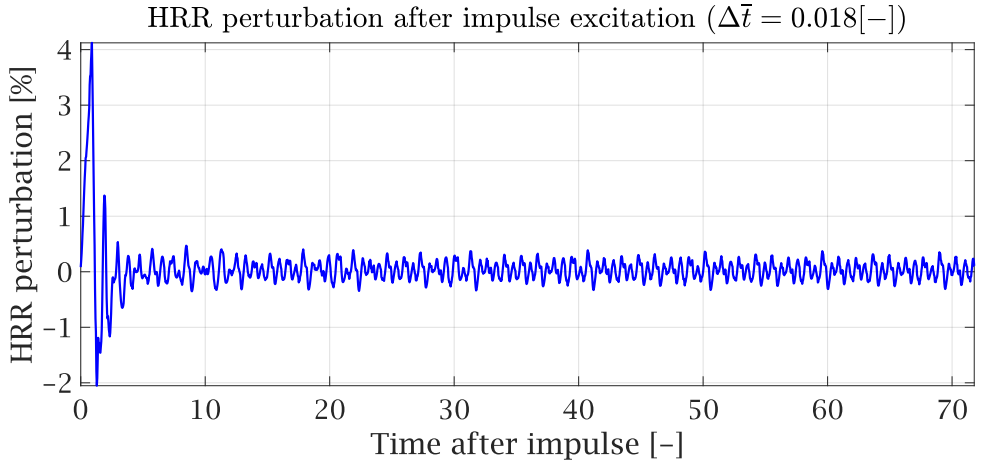

Figure 5.5: Heat release rate fluctuations of the impulse excitation simulation. The time step used in the transient simulation is $\Delta\bar{t} = 0.036$. Periodic behaviour is observed after approximately $\bar{t} = 21.5$.

An overshoot in the HRR can be seen after the impulse, followed by an undershoot. The overshoot and undershoot are approximately twice as high compared to the result seen in Figure 5.3. This could be due to an overestimation in the simulation resulting from the increased time step. The impulse dampens rapidly to periodic behaviour, however this signal is not similar to the result from the unexcited system (see Figure 5.1). For the FTF, all time steps before $\bar{t} = 21$ are considered. As such, the lowest frequency in the FTF is $St_{min} = 1/21 = 0.0476$.

The normalized flame transfer function is shown in Figure 5.6. A reference value is chosen to normalize the FTF for comparison with the other methods. Here, the value is chosen where the phase crosses the 0 rad line ($St = 0.0928$). This is chosen, as the phase diagram shows expected behaviour for frequencies above this value, namely an approximately linear phase shift.

The FTF from the $\Delta\bar{t} = 0.036$ simulation can be compared with the result from the $\Delta\bar{t} = 0.018$ simulation. While both FTFs show similar (approximately low-pass filter) behaviour, the locations of the peaks in the gain are shifted. The lower frequencies are shifted less than the higher frequencies, similar to the spectral analysis in Figure 5.4. The biggest difference is seen in the peaks at $St = 1.48$ and 1.67. This shift here cannot be explained by a time discretization error. It might be the result of the difference in periodic behaviour after the flow has settled. As the peak at $St = 1.48$ of the $\Delta\bar{t} = 0.036$ result is not in phase, it is not expected that this will influence the stability of the system significantly. Oscillations with a frequency $St > 2$ are damped out in the flame, apart from some specific oscillations intrinsic to the flame.

The gain is found to be approximately higher than 1 for the frequencies $0.1 \leq St \leq 0.9$ for $\Delta\bar{t} = 0.036$. This is a result of the reference value used. The peaks in the FTF around $St = 1.05$ is comparable between the two simulations. These peaks are not a significant frequency in the

unexcited system. The FTF's presented here will be implemented in the ANM for full comparison with the other FTF's.

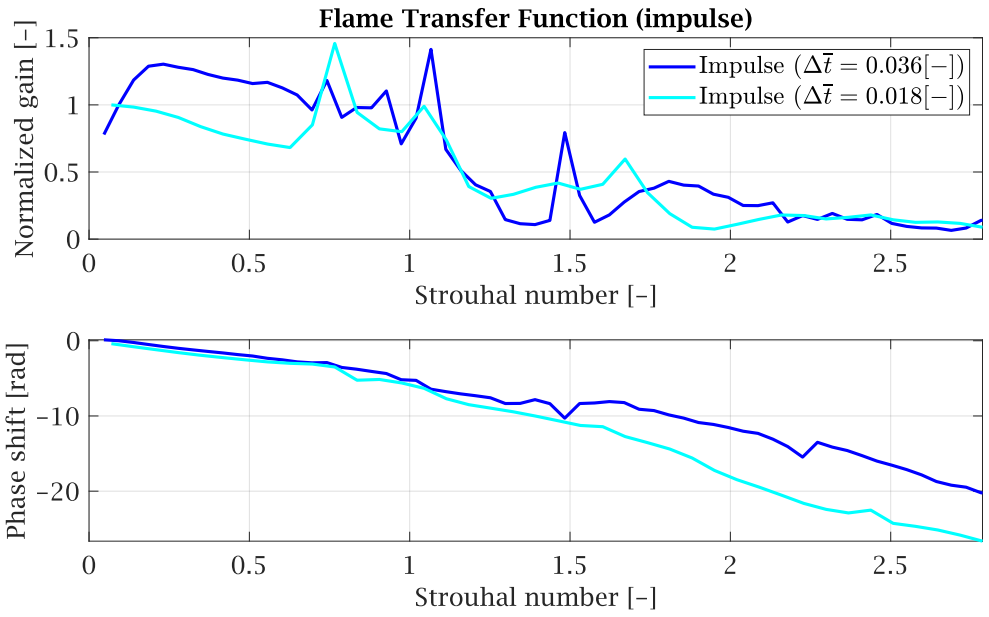

Figure 5.6: Flame transfer function obtained from an impulse excitation transient simulation with $\Delta\bar{t} = 0.018$ and $\Delta\bar{t} = 0.036$. For the former FTF, all time step results for $\bar{t} \leq 15$ are considered. The gain is normalized with the first value at $St = 0.07$. For the latter, all time step results for $\bar{t} \leq 21$ are considered. The gain is normalized with the point where the phase crosses 0 rad.

Comparison of FTFs from full transient runs

The full transient runs can also be analyzed and FTFs can be computed (see Figure 5.7). The resulting FTFs is similar to the graph shown in Figure 5.6, but the resolution is higher as more time steps are used in the computation. In addition, the low frequency behaviour is visible. For frequencies $St < 0.017$ for the $\Delta\bar{t} = 0.036$ result, the gain rises significantly. This is most likely due to the low frequency behaviour of the flame as seen in the unexcited system (see Figure 5.2). These low frequencies are not obtained in the $\Delta\bar{t} = 0.018$ FTF, as the simulation time was too short. In the full FTFs, additional peaks can be seen, that approximately correspond to the peaks seen in Figure 5.2. These frequencies do not show in the FTFs from Figure 5.6, as the time considered for those coarse FTFs is too short. The oscillations corresponding to these new peaks are present, but they do not occur often enough to show up significantly in a spectral analysis. The phase shifts of the two FTFs are comparable, although the full simulation result shows more jumps at the intrinsic frequencies with a high gain. At normalized frequencies $St > 1.6$, the phase lines differ by approximately 2π rad.

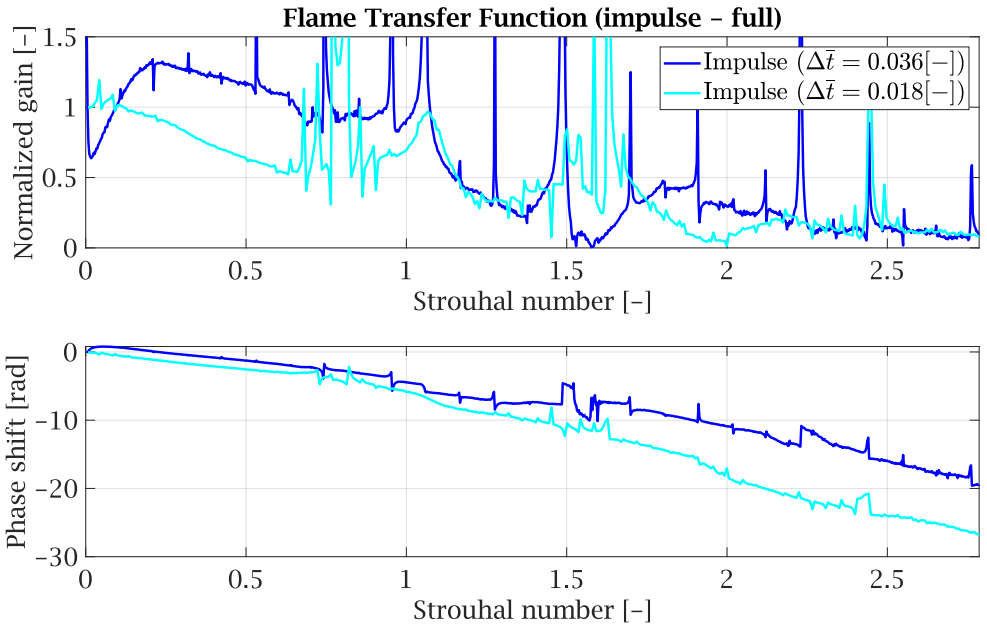

Figure 5.7: Flame transfer function obtained from the full impulse excitation simulations. The $\Delta\bar{t} = 0.018$ FTF is normalized with the first value; the $\Delta\bar{t} = 0.036$ FTF is normalized with the value at the highest frequency for which the phase crosses 0 rad. This result is not used in the acoustic network models.

5.1.2 White noise excitation

The white noise excitation simulation is run with a $\Delta\bar{t} = 0.018$. The excitation signal is changed every 10 time steps based on a pseudorandom number generated set of values. The volume integrated HRR is sampled at the start of these new excitation[2], resulting in a sampling frequency $St = 5.57$. As such, the highest frequency considered in the white noise FTF is the Nyquist frequency, $f_N = f_s/2 = 2.79$. The simulation is run for $\bar{t} = 700$.

Bin parameters

To obtain an FTF with a white noise simulation, an averaging procedure is used. The full set of HRR data is divided into subsets called bins. These bins have a length shorter than the full set and overlap each other by a margin. The choice in these parameters (length and overlap) influence the quality of the FTF. Fewer bins increase the length of each dataset, resulting in a lower f_{min} in the FTF and increasing the resolution. In addition, this can increase the coherence of the result. It does introduce more irregularity in the FTF, such as additional peaks. This is shown in Figure 5.8, where the FTF obtained by taking 12 bins (with 75% overlap) is smoother than the FTF found using 3 bins.

In this work, 12 bins are chosen with 75% overlap (Black line in Figure 5.8). This choice is made

[2]The sampling frequency is high enough to obtain a negligible difference in the FTF compared to sampling at the end of the excitation.

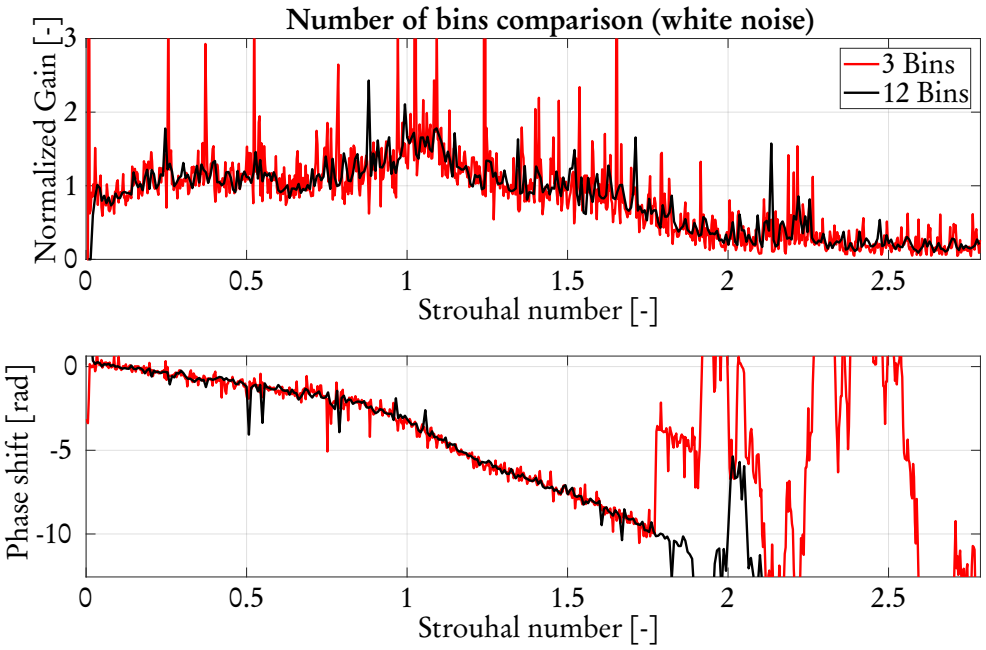

Figure 5.8: Flame transfer functions obtained from white noise simulations using different number of bins. 75% overlap of the bins is used. The bins simulate for an effective time of $\bar{t}_{3\text{ bins}} = 355.3$ and $\bar{t}_{12\text{ bins}} = 142.1$. The gain is normalized using a normalization factor of 1.5.

based on the quality of the FTF and the coherence. Fewer bins would increase the coherence, but it would result in an FTF with less readability. More bins would smooth the FTF at the expense of the coherence of the result.

Comparison to impulse

The white noise excitation FTF can be compared against the impulse FTFs. This is shown in Figure 5.9. The gain of the FTF has an overall low-pass filter shape. The gain increases around $St = 1.05$; for higher frequencies, the gain reduces. This is similar to the result from the impulse excitation simulations. The difference lies in the gain after the peak, where the white noise FTF is near unity (similar gain to low frequency behaviour). The impulse FTFs fall off sooner to a lower gain. In other words, the (normalized) corner frequency for the white noise FTF is $f_{c,whitenoise} = 1.5$, while for the impulse FTFs $f_{c,impulse} = 1.1$.

When comparing the phase shifts, a more significant difference is present. Around $St = 1.05$ where the FTFs show a peak, the phase difference between impulse and white noise is approximately π rad. As such, the peak is in phase for the impulse FTFs and out of phase for the white noise FTF. The slope of the phase is similar until 1.85, where the white noise phase behaves chaotically. This can be explained when considering the coherence γ^2 of the white noise FTF (see Figure 5.10), computed using Equation 3.6.

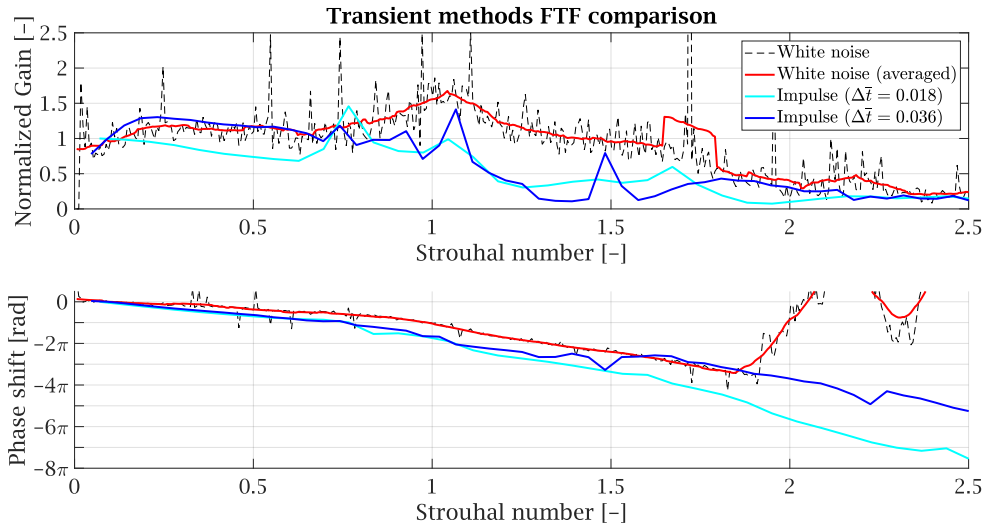

Figure 5.9: Normalized flame transfer functions determined using transient methods: White noise ($\Delta\bar{t} = 0.018$) and Impulse ($\Delta\bar{t} = 0.018$ and $\Delta\bar{t} = 0.036$) excitation. A moving average (centered window of 25 points) is applied to the white noise FTF (red line) to show its behaviour more clearly.

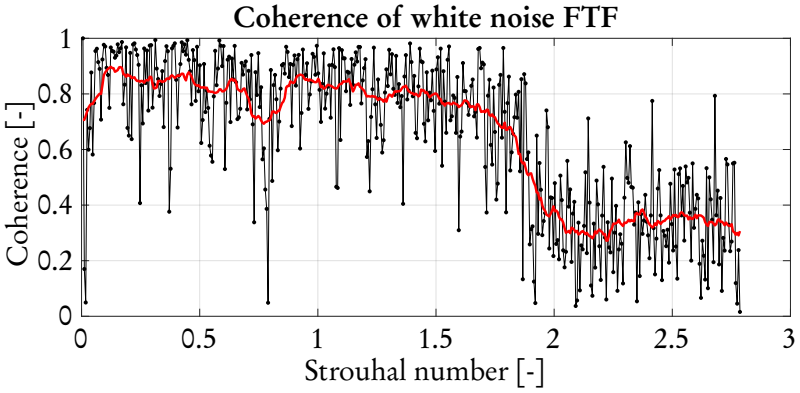

Figure 5.10: Coherence of the white noise flame transfer function, showing the degree of linearity. A value less than unity shows the presence of non-linearity, leakage and noise. The red line shows a moving average of the coherence values.

The coherence drops significantly for frequencies $St > 1.9$. The presence of noise could be the reason for this drop as the gain is close to zero for these frequencies. If the excited signal strength is low, random noise can have a more significant influence on the FTF.

5.1.3 Linear coefficient method

To compare the transient methods against a steady state method, FTFs are generated using LCM. The resulting FTFs obtained using the 3D LCM code with the UT-FGM combustion model are shown in Figure 5.11. The parallel computing implementation was used to reduce the computation

time (see Section 5.1.4). The LCM FTF gains are normalized using the lowest frequency gain. The impulse excitation ($\Delta\bar{t} = 0.018$) FTF is shown to compare the results.

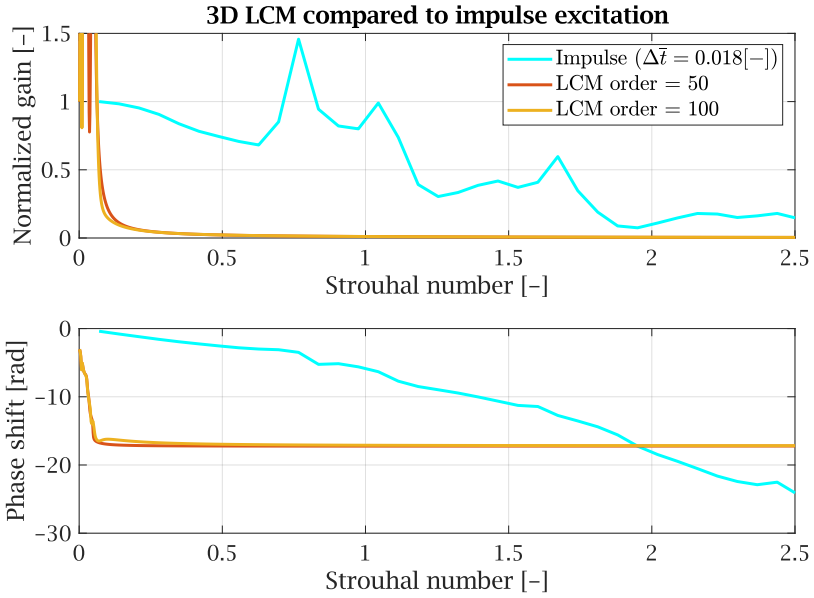

Figure 5.11: Flame transfer functions obtained using 3D LCM (6 fluctuated variables). Two reduced order models are shown. The impulse FTF (Figure 5.6) is shown for comparison.

Figure 5.11 shows both the gain and the phase of the LCM result differ from the transient method result. The normalized gain approaches zero at $St \approx 0.5$ for both LCM FTFs. Similarly, the phase reaches a near constant value of -17.1 rad at $St \approx 0.1$. The slope of the phase shift before this normalized frequency is steeper than the impulse result.

As such, the implementation of LCM used in this work seems to fail to find an FTF that approaches the behaviour of the FTFs obtained with the transient methods. To investigate this, several computations are run on different meshes and with different parameters. The different meshes all resulted in similar looking FTFs for LCM as shown in Figure 5.11.

For the previous result, 6 variables were fluctuated: 3 speeds ($\boldsymbol{u}$), enthalpy (h), the reaction progress variable (c) and the mixture fraction (f). Selecting only the f or the f and RPV resulted in similar results (see Figure 5.12). The reduced order model $k = 500$ shows a non-zero gain for higher Strouhal numbers, but the FTF is dissimilar to the impulse FTF.

2D LCM

To investigate if the issue for the dissimilar FTFs results from the parallelization in the computation of the matrices, 2D LCM computations can be done to compare the result. Although the results will not be exact, as the domain is not axisymmetric, it can give an indication as to what gives the previous result. The time scales for computing 2D cases in LCM are sufficiently small to allow computation without a parallel scheme.

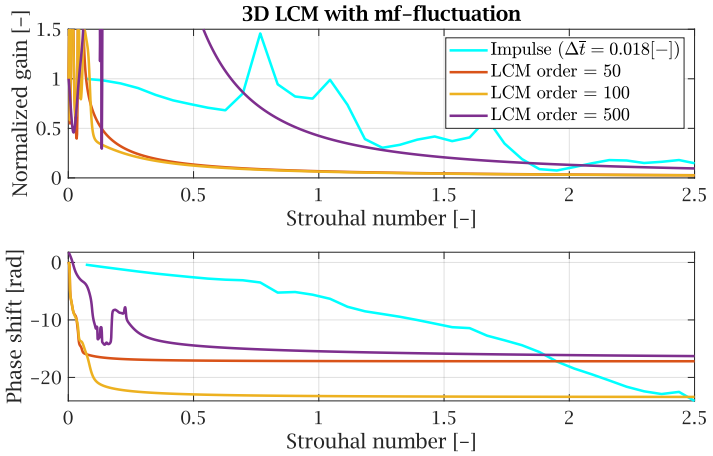

Figure 5.12: Flame transfer functions obtained using mf-fluctuations in 3D LCM. Three reduced order models are shown. The impulse FTF (Figure 5.6) is shown for comparison.

The computational domain has two symmetry boundary conditions. The 2D-code was run for both boundary conditions and resulted in similar behaviour. The obtained FTFs for one of the boundaries is shown in Figure 5.13. Similar to the 3D case, higher orders for the reduced model result in a non-zero gain for higher Strouhal numbers, however the result is dissimilar from the expected behaviour.

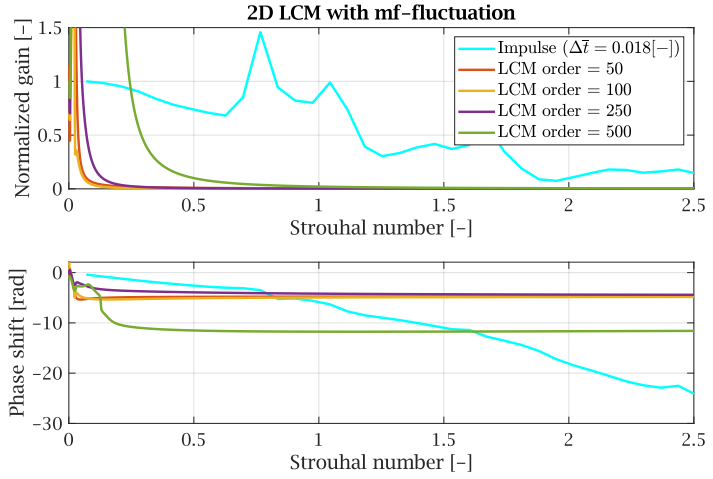

Figure 5.13: Flame transfer functions obtained using mf-fluctuations in 2D LCM. Four reduced order models are shown. The impulse FTF (Figure 5.6) is shown for comparison.

The used implementation of LCM does not provide satisfactory results and will not be compared with the ANM. The following parameters were changed to obtain a usable FTF (without success):

- The frequency shift in the shifted Lanczos step: The frequency shift is used in the reduced order model essentially as a Taylor's expansion around the selected frequency. In the Figures

above, the $\boldsymbol{A}$-matrix is shifted by 2π rad. Choosing values higher than this, such as a value near $St = 1.1$ where the transient methods showed a unique peak due to the forcing, resulted in singular matrix warnings when computing the reduced order system. Only low values of this shift parameter appeared to give any result.

- The order of the reduced systems: The matrices generated in LCM are too big to solve the state space system for all frequencies (sparse $\boldsymbol{A}$-matrix in the order of 1M by 1M). The system is reduced essentially by projecting the state space system on a reduced order system. Higher orders will approach the original matrices behaviour. Increasing the order is more computationally expensive, sometimes exceeding hardware limits. In addition, it was found to occasionally result in undefined eigenvalues ('Not a Number' in Matlab).

- Size of the domain: For most of the LCM computations, the number of control volumes are filtered to only consider the relevant locations near the flame. This is done to limit the computational expense. For the 3D simulations, the filters included a radial location filter and a volumetric heat release rate filter. The former is to consider only points near the flame front/inlet; the latter is to limit the number of control volumes in this region where the flame is not active[3]. In the 2D LCM computations, all nodes could be considered on the symmetric BCs, still resulting in poor FTFs.

- Different combinations of fluctuated variables: An effort was made to consider different combinations of fluctuated variables to see if the results would change. The mixture fraction is fluctuated in all LCM computations. Adding the reaction progress variable or enthalpy did not influence the FTF in a meaningful manner. The gain reached a near-zero value before $St = 0.3$ and the gain approached a constant value in most cases. Excessive spikes could be seen in the gain (and in some cases the phase), which is unlike the flames behaviour at low frequencies. This was tested on the 2D and the 3D LCM code.

5.1.4 Computation time

A comparison between the different methods can be made based on the computation time required to obtain the FTF. The order of computation time is stated here for this specific mesh (see Table 5.1).The initial time to obtain a steady state simulation result is not incorporated, as all methods used the same result to determine the FTF. The impulse excitation simulations did have an initial simulation time to allow the solution to 'settle' to the transient solution, although this is negligible compared to the full computation time. Applying the impulse excitation in the settling causes the impulse to effectively be ignored. For the white noise result, this is less important, as the flow is constantly excited. In addition, a Hanning window is applied to the bins, which has the effect of damping the initial settling of the first bin.

The impulse excitation simulations only need to be simulated until the oscillations return to levels equivalent to the noise in the simulation. As such, the full transient simulations taking over a week to finish is not required. Rather, the required computational cost is only 3 to 5 days. This is however not a priori knowledge, meaning a longer simulation time can be required for certain cases. Here a near laminar flame dampens the oscillations relatively quickly, but this might not be

[3] As the heat release rate at the inlet is near zero, these nodes are ignored as well using this filter. It should be noted that considering these inlet nodes as well did not result in a significant change in gain or phase of the FTF. The FTFs still looked comparable to the result shown in Figure 5.11.

Table 5.1 Approximate computation times for the different methods for obtaining a flame transfer function.

Method	Time	Note
Impulse	$\sim$ 12 days	$\Delta\bar{t} = 0.018$, $\bar{t}_{max} = 270$
	$\sim$ 5 days	$\Delta\bar{t} = 0.018$, $\bar{t}_{max} = 15$
Impulse	$\sim$ 8 days	$\Delta\bar{t} = 0.036$, $\bar{t}_{max} = 360$
	$\sim$ 3 days	$\Delta\bar{t} = 0.036$, $\bar{t}_{max} = 21.5$
White noise	$\sim$ 4 weeks	$\Delta\bar{t} = 0.018$, $\bar{t}_{max} = 720$
LCM	$\sim$ 1 day	342473 control volumes, 6 fluctuated variables
	$\sim$ 1 day	Restarted Lanczos order reduction

the case for more turbulent flames. To save on computational effort, monitoring of the HRR in progress is required such that the simulation can be stopped sooner.

A big difference in computation time is observed between the white noise and the impulse simulations. As the white noise excitation method requires averaging over multiple bins, longer simulation time is required for this method. The impulse excitation method only requires simulation until the HRR fluctuations have reduced to the noise levels. In addition, each time step on average requires more coefficient loops. As the inlet conditions are constantly changing for the white noise simulation, convergence in the simulation requires more coefficient loop computations.

The computational resources for the methods used here are not identical. The transient methods used 36 physical cores[4] (hyper-threaded to 72 logical cores) and 72 GB of RAM. The LCM Matlab code was run on 32 logical cores[5] with RAM in excess of 700 GB (dependent on the required matrix reduction and number of fluctuated variables). Due to the constraints in Matlab, a large part of the LCM code is a single threaded operation. Calculation of the coefficients is parallelized and can, if the hardware supports this, be run on more than 32 cores for increased speed. In addition, further speed improvements can be made by parallelizing the calculation of the reference matrices, although this effect on computation time is minor compared to the computation of the coefficient matrices.

The time for computing the coefficient matrices depends on the number of control volumes and the number of fluctuated variables. For every control volume, the LCM code loops over all fluctuated variables to compute the coefficients. As such, the computation time is influenced by these parameters. A selection of approximate computation times[6] is shown in Table 5.2 for different combinations of number of control volumes and fluctuated variables. It is found the number of control volumes seem to have the most significant influence on the computation time. Adding additional fluctuated variables, such as velocity $\boldsymbol{u}$ and enthalpy h, has little impact comparatively.

[4]The computer node has 2 Intel® Xeon® Gold 6140 Processors [15]

[5]The computer node uses 4 Intel® Xeon® Processor E7-8890 v4 Processors [16]; 32 were used as this is a limit set on the parallel computing in Matlab on this cluster.

[6]For some combinations of control volumes and fluctuated variables, the computation was repeated. The duration seemed to vary at most 30 minutes. Due to the small number of repeated computations, no significant conclusions can be drawn on the variance in duration. The result is also clock speed dependent, which was not measured during computation.

Table 5.2 Approximate computation time of $\boldsymbol{A}$ and $\boldsymbol{C}$-matrix coefficients in the parallel 3D LCM FGM-implementation. Different number of control volumes and fluctuated variables are used. For these computations, 32 parallel cores were used.

Control volumes	Fluctuated variables	Duration (h)
153008	f	~ 2
153008	c, f	~ 3
182545	$\boldsymbol{u}$, h, c, f	~ 4
245634	$\boldsymbol{u}$, h, c, f	~ 7
342473	$\boldsymbol{u}$, h, c, f	~ 15.5

5.2 ACOUSTIC NETWORK MODEL SENSITIVITY STUDY

The FTFs can be imported into the ANM and converted using Equation 4.33. The network structure from 4.5 can be tested and a sensitivity analysis can be performed. The following effects are analysed using the impulse ($\Delta\bar{t} = 0.018$) FTF: changing the impedance BC at the heat exchanger; adding a volume element upstream of the flame holder; changing the turbulent damping coefficient. After, the different FTFs will be compared.

5.2.1 Effect of impedance BC at heat exchanger

A scaled (dimensionless) impedance ζ is set at the inlets and outlets of the domain. On the inlets, the value is set a sufficiently large value to reflect all sound waves without a phase shift ($\zeta \to \infty$). A fan is located at the air inlet, so full reflection is assumed. As the hydrogen inlet is small, full reflection is assumed here as well. At the heat exchanger exit, an additional impedance ζ_{hex} should be set. This value has a more direct influence on the acoustic behaviour, compared to the inlets. The flame holder acts as an acoustic damper due to the significant flow constriction, so this effect is more important than the upstream effects at the inlets.

For $\zeta = 0$, acoustic waves are reflected with a 180° phase shift. $\zeta = 1$ results in no reflection of the incoming waves; $\zeta \to \infty$ results in full reflection. The pressure and stability diagrams are shown in Figure 5.14.

For values $\zeta_{hex} \geq 1$, the pressure plot looks similar except for the low frequencies where the pressure perturbation of $\zeta = 1$ falls off to 138 dB. The pressure perturbation at the flame has a peak at $St = 0.15$. The peak for $\zeta = 0.1$ is at 0.14, with a reduced pressure perturbation for lower frequencies and an increased pressure for higher Strouhal numbers. Around this frequency, the element matrix $\boldsymbol{A}$ is singular, as seen in the stability plot. This frequency is similar for all eigenvalues of $\zeta \geq 1$, however the imaginary part ω_i of the frequency differs. Following from Equation 2.3, the ratio of ω_i to ω_r determines the speed at which oscillations dampen out or grow in time. For an identical ω_r, an increasingly positive ω_i results in faster damping. As such, when acoustic waves are not reflected ($\zeta = 1$), the oscillations dampen out more quickly. The position of the complex frequencies differs little for other values of ζ, and the system does not gain an instability as a result of a changing ζ_{hex}.

A value of $\zeta_{hex} = 10$ will be used as a balance between the reflection due to the significant area constriction at the combustion chamber exit (reflecting incident waves, $\zeta \to \infty$) and the pass

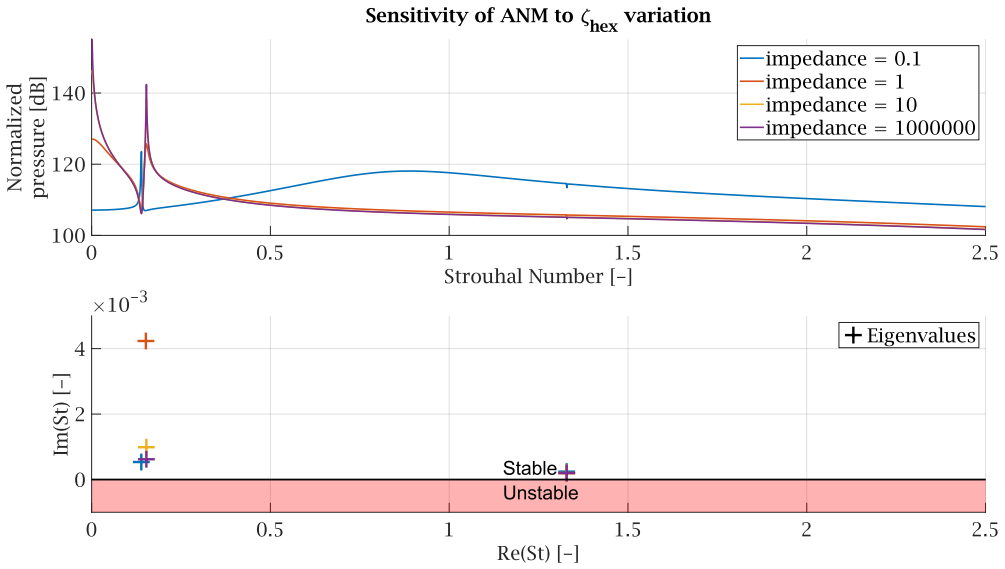

Figure 5.14: Pressure perturbation (top) and stability (bottom) diagrams for varying impedance values at the heat exchanger in the acoustic network model. The impulse ($\Delta\bar{t} = 0.018$) FTF is used to obtain these diagrams. The pressure perturbation is shown at the flame node in the combustion chamber. The eigenfrequencies (crosses in the stability plot) correspond to the complex frequencies for which $\det|\boldsymbol{A}| \downarrow 0$.

through of flow out of the domain (no reflection, $\zeta = 1$). The real part of the eigenvalues is not affected by $\zeta \geq 1$, therefore the choice is somewhat arbitrary and different values can be chosen. A real value for the impedance should be measured on the real system.

5.2.2 Effect of adding volume element upstream of flame holder

The ANM shown in Figure 4.5 can be adapted to use a volume element. Based on the geometry[7], this could be chosen to construct the network model. This network structure is shown in Figure 5.15. In the ANM code, this volume is modeled as an inviscid volume, which ignores the turbulent effects in the location of the volume. The pressure and stability diagrams are shown in Figure 5.16. The data from Figure 5.14 ($\zeta_{hex} = 10$) is shown for comparison.

With the addition of the volume element, the eigenvalue at $St = 0.15$ is shifted to $St = 0.45$. As a result, the peak in the pressure perturbation plot is removed, resulting in a smoother response. For higher Strouhal numbers, the pressure behaviour is similar. The eigenfrequency at $St = 1.3$ is nearly unaffected. As the mean flow in the position of the volume is turbulent, the inviscid volume element might be less accurate. As such, in the comparison of the FTFs, the model without the volume element is used.

[7]Not shown here for reasons of confidentiality.

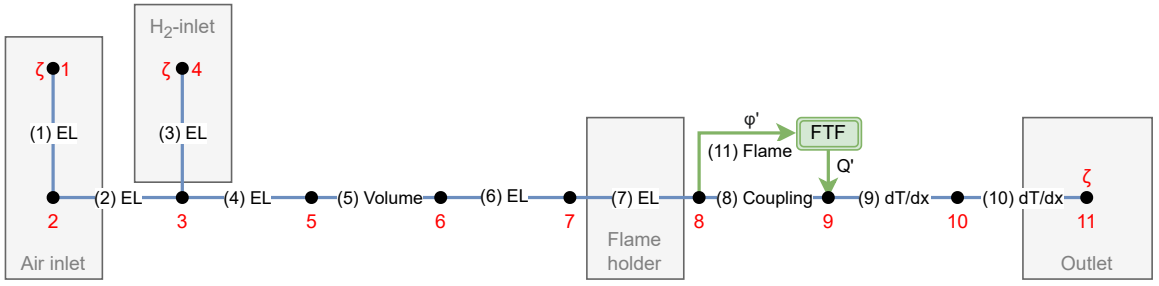

Figure 5.15: Schematic overview of the acoustic network model with a volume element (element 5) upstream of the flame holder. The nodes (black dots with red index) are connected by 1D elements (blue lines with element number and types). Impedance boundary conditions ζ are applied at the inlet and outlet nodes.

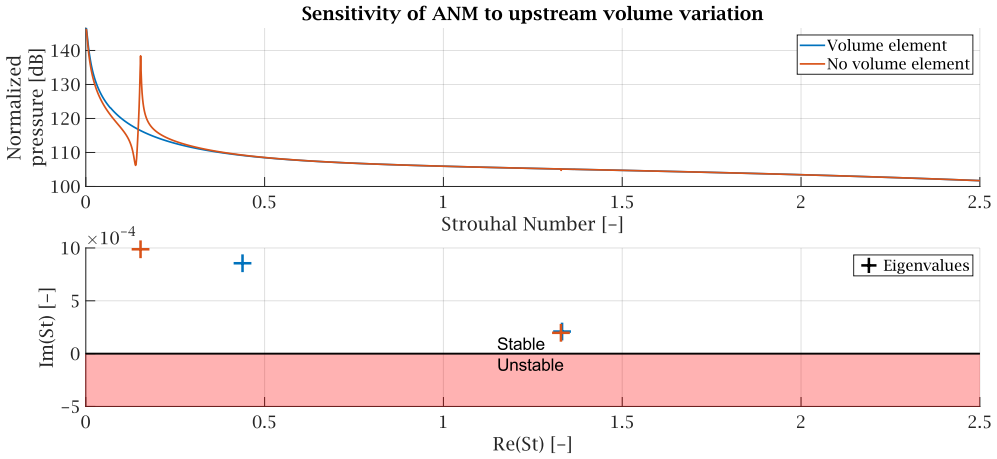

Figure 5.16: Pressure perturbation (top) and stability (bottom) diagrams comparing the effect of a volume element upstream of the flame holder. The impulse ($\Delta\bar{t} = 0.018$) FTF is used to obtain these diagrams. The pressure perturbation is shown at the flame node in the combustion chamber. The eigenfrequencies (crosses in the stability plot) correspond to the complex frequencies for which $\det|\boldsymbol{A}| \downarrow 0$.

5.2.3 Effect of turbulent damping coefficient

The 1D tube elements account for acoustic damping by considering a pressure drop due to turbulent friction. For low mach numbers of the mean flow, this is a reasonable approximation. The turbulent friction is found with a turbulent damping coefficient β_t (Equation 4.30). β_t can be scaled to analyze the effect of this parameter on the stability. This effect is shown in Figure 5.17 where all turbulent damping coefficients are scaled with the 'Scaling Factor.'

It can be seen from this figure the real part of the eigenvalues is unaffected; only the imaginary part is shifted. Increasing values of the scaling factor increases the turbulent damping in the system. Logically, the imaginary part of the eigenvalues increases in magnitude, as this is a measure of the speed with which oscillations are damped. Additionally, the peak in the pressure perturbation plot is lower for higher scaling factors.

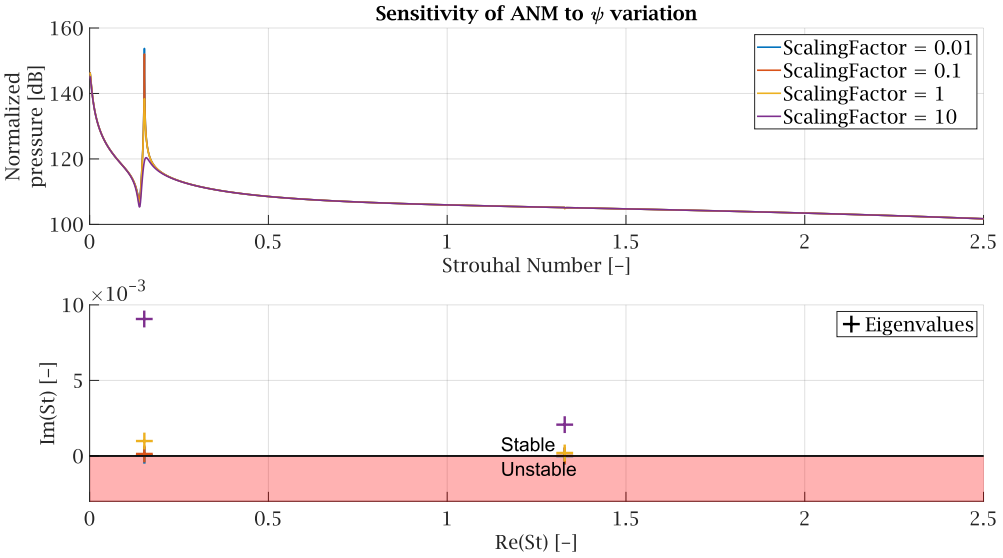

Figure 5.17: Pressure perturbation (top) and stability (bottom) diagrams for varying turbulent damping scaling factors. The impulse ($\Delta\bar{t} = 0.018$) FTF is used to obtain these diagrams. The pressure perturbation is shown at the flame node in the combustion chamber. The eigenfrequencies (crosses in the stability plot) correspond to the complex frequencies for which $\det|\boldsymbol{A}| \downarrow 0$.

In a zoomed view of the eigenvalues, interesting behaviour can be seen (Figure 5.18). When the scaling factor equals 0.01, an unstable eigenvalue arises. When the amount of turbulent damping is reduced by two orders of magnitude, the system lacks sufficient acoustic damping to remain stable. Considering this occurs when β_t is scaled by 0.01, the stable eigenfrequencies for scaling factor=1 are accepted.

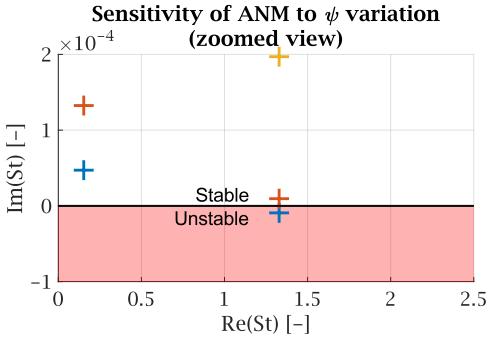

Figure 5.18: Zoomed view of the stability plot from Figure 5.17. The crosses are eigenvalues of the system. When the turbulent damping coefficient scaling factor equals 0.01 (blue crosses), an unstable eigenfrequency is observed.

5.2.4 Comparison of flame transfer functions

The three FTFs obtained using the transient methods are implemented in the ANM. The values of the FTF are known at discrete frequencies following from the method of computing the FTF. In the ANM code, the discrete values of the gain and phase are stored in a vector. Linear interpolation (using Matlabs `interp1( )` function) is used to find the intermediate values. A pressure perturbation and stability plot is generated to qualitatively compare the FTFs in the model (see Figure 5.19). All obtained eigenfrequencies are stable. The three different FTFs produce com-

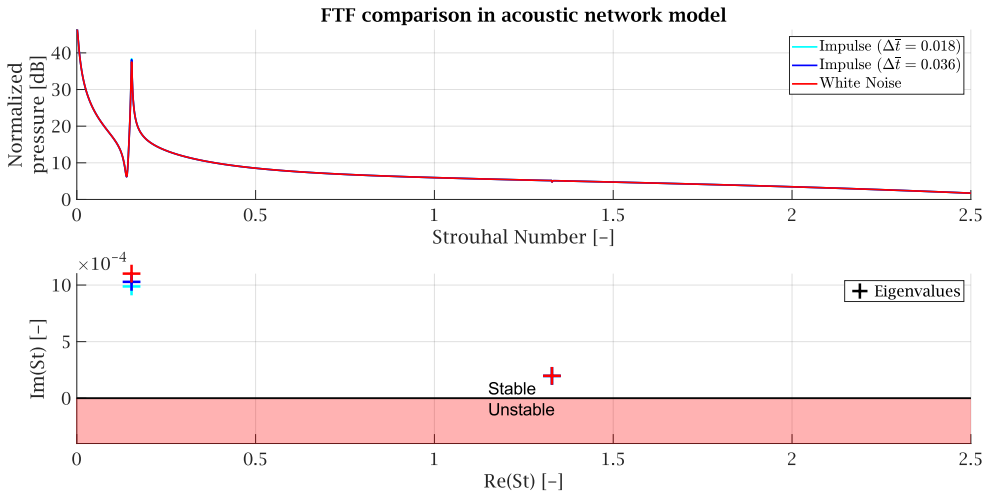

Figure 5.19: Comparison of flame transfer functions implemented in an acoustic network model. Pressure perturbation (top) and stability (bottom) diagrams show the characteristics of the acoustic network model (Figure 4.5). The eigenfrequencies (crosses in the stability plot) are stable for all FTFs compared here.

parable results in the stability plot. In the pressure perturbation plot, the normalized pressure is identical for the different methods. Consequently, the residential condensing boiler appears stable given the simulation parameters.

The difference between the FTFs (Figure 5.9 results in a change in the damping of the eigenfrequencies. The real part of the lower eigenfrequencies is identical between the methods ($St = 0.153$ and $St = 1.329$). The imaginary part shows a higher damping for the white noise FTF compared to the impulse FTFs. This aspect can be quantified by the growth rate GR (Equation 2.3). Table 5.3 shows the growth rate comparison of the eigenvalues at $Re(St) = 0.153$. The growth rate is

Table 5.3 Comparison of growth rates of the lowest eigenfrequency obtained for the different Flame Transfer Functions (FTFs) in the acoustic network model. The percentage difference is relative to the impulse ($\Delta\bar{t} = 0.018$) result.

FTFs	**Growth rate** GR	**Difference** [%]
Impulse $\Delta\bar{t} = 0.018$	-0.0397	-
Impulse $\Delta\bar{t} = 0.036$	-0.0413	4.00
White noise	-0.0442	11.21

negative for all eigenfrequencies, showing oscillations will dampen out in time. Compared to the

impulse ($\Delta\bar{t} = 0.018$) result, the white noise FTF results in an eigenfrequency with a growth rate 11.21% higher. This may be due to the phase shift at the peak in normalized gain at $St = 1.05$ (Figure 5.9). The phase shift of the white noise result is π rad, whereas the impulse excitation FTFs have a phase shift around 2π rad. As such, the white noise result is deconstructively interfering with an applied perturbation; the impulse FTFs show constructive interference based on the phase shift.

Chapter 6

Discussion

This chapter discusses the results based on the validity of the CFD model (Section 6.1, 6.2 and 6.3) and the LCM implementation (Section 6.4). The chapter closes with a discussion of the obtained stable eigenfrequencies by evaluating the expected first eigenfrequency of the combustion chamber (Section 6.5).

6.1 EXPERIMENTAL VALIDATION OF RESULTS

The CFD simulations in this work have not been validated with experimental results. Care should be taken when interpreting the results. A converged solution does not imply a correct result, as seen in the choice in combustion model (see Section 4.1.2). Depending on the model parameters, different solutions can be obtained. These should be checked with theory or experiments.

LCM has been checked with experimental results in [38] and is compared against the same transient methods used in this work. The method shows acceptable agreement with experimental results for a swirling turbulent flame. The UT-FGM model has been compared with experimental results for a premixed jet flame [13]. Based on laminar flame theory, the flame thickness was computed and good agreement was found with the FGM combustion model. As such, it is expected the implementation of FGM in the LCM results in a valid flame, but experimental results are required to verify this.

A matter ignored in the simulation is the preferential diffusion of hydrogen as this has not been added to the CFX implementation of UT-FGM (see Section 6.2). In addition, adiabatic walls were used in this work due to time constraints. An experimental setup will have heat transfer to the walls of the system, which can influence the flame. With a wall temperature boundary condition, the flame can be lifted from the wall, which will influence the FTF [4]. The flame will heat up the flame holder in the experimental setup, such that the actual flame might be lifted and a different FTF can be obtained.

6.2 PREFERENTIAL DIFFUSION EFFECTS

An aspect not considered in the simulations is the preferential diffusion effect of hydrogen. Hydrogen has a stronger mass diffusivity compared to thermal diffusivity ($Le << 1$ in a hydrogen-air mixture). Resulting from this, the species is transported differently from the unity-Lewis fluid simulated in FGM. Adaptations to the Ansys CFX implementation of UT-FGM are required for this

effect to be considered.

If preferential diffusion is modelled, hydrogen will transport to lower hydrogen concentration regions. This can result in a wider flame and can alter the flame tip, as in [28]. The heat release rate maximum will shift towards the root of the flame rather than the tip. As the prevalent thermoacoustic modes in the near-laminar flame are longitudinal, it is not expected this preferential diffusion effect is significant in determining the FTF. This should be confirmed by comparing accurate simulations with experimental results.

6.3 POROUS MEDIUM

The real flame holder contains multiple holes for the combusting mixture to pass through. The flame forming in the combustion chamber is directly influenced by these holes. In this work for reasons of simplicity, this region of the model was modeled as a porous medium. This method preserves the pressure drop across the region but it does not model the individual holes. As such, parameters such as turbulence, species mass fraction and velocity are not entirely accurate. The flame shape resulting from this modeling choice is different from the actual expected flame shape. In simulation, a V-shaped flame is observed (as in Figure 4.1), while in the real system every hole would have a V-shaped flame.

Interaction between these individual flames is not considered, nor is the flame length used here entirely accurate. As a qualitative comparison of the transient methods, this consequence is acceptable. The mesh refinement required to model the individual holes in the combustion chamber would be too great for this analysis. To overcome this issue, flames in these individual holes can be simulated with the appropriate boundary conditions. An FTF of this subsection can be obtained and compared to the FTFs obtained in this work (which use a porous medium).

6.4 LCM IMPLEMENTATION

The current LCM implementation does not give accurate results yet for this residential condensing boiler case study.[1] The method has been shown to work using the FR/EDM model with the DESIRE burner configuration [38], so the root of the problem is assumed to be in the FGM implementation.

The LCM implementation uses a first-order upwind advection scheme. This method introduces artificial dissipation to the system, resulting in inaccurate results. As such, the method needs to be adapted to use a high-resolution advection scheme. When the method is used to compare the FTF from a high-resolution steady state solution to a first-order upwind scheme for the DESIRE burner, a difference in gain and phase of the FTF can be seen (Figure 6.1). The gain is higher for the upwind advection scheme. The frequency of the peaks in the normalized gain matches between the two solutions. Consequently, to more accurately find the gain in the FTF, a high-resolution advection scheme should be used in LCM. The phase shift is similar, although the upwinding scheme estimates a slightly larger time delay. This may be due to the additional dissipation in the system smearing out the flame front.

[1] The exact reason for this is unknown at the time of writing.

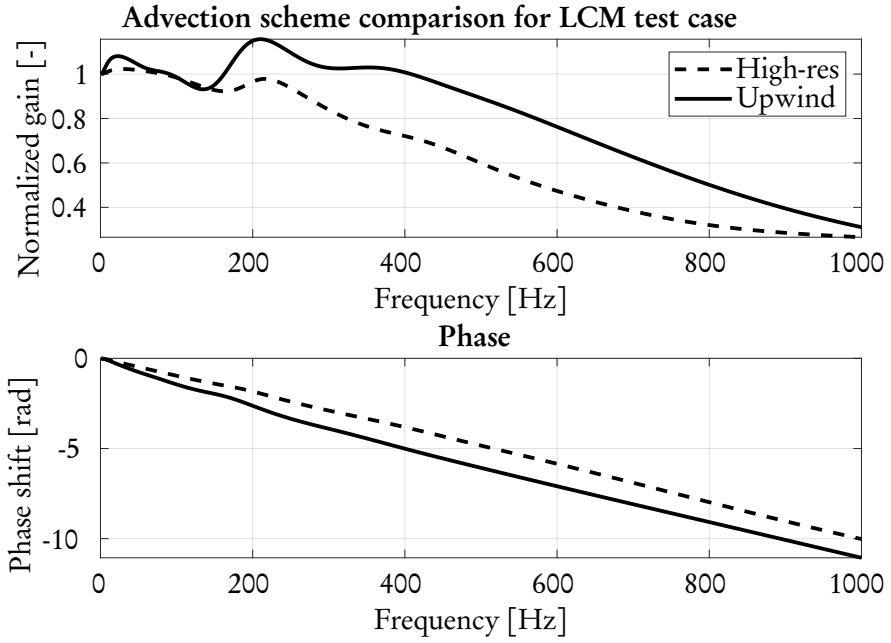

Figure 6.1: Comparison of the flame transfer function obtained using LCM with a steady state solution using different advection schemes. The methane-fuelled, swirling DESIRE combustor is used for this analysis [38].

6.5 INTRINSIC THERMOACOUSTICS

The hydrogen-fuelled condensing boiler examined in this work appears stable based on the FTF's obtained from impulse and white noise excitation. This may be an expected result considering the length of the combustion chamber. The first acoustic eigenmode is approximately equal to the first eigenmode of a 1D tube, found by

$$f = \frac{c_0}{2L} \tag{6.1}$$

where c_0 is the local speed of sound and L is the length of the tube (here the length of the combustion chamber inlet to outlet). Consequently, the first acoustic mode has a non-dimensional frequency of $St = 8.8$. At these normalized frequencies, the low-pass behaviour in the FTF has dampened out the excitation. Consequently, it is not expected an extrinsic thermoacoustic coupling will cause an instability. Intrinsic instabilities of the flame might be more important for similar systems, due to the relatively small combustion chamber. Intrinsic combustion instabilities do not rely on reflection of acoustic waves. Rather, the acoustic waves generated by the unsteady HRR perturb the flow upstream of the flame [11]. This perturbation is convected to the flame front, where the combustion is affected. This changes the HRR, which in turn changes the acoustic waves that travel upstream.

In industrial boilers, the reflection of acoustic waves might be more important than the residential condensing-boiler examined in this study, as the length scale is larger. Increasing the length in Equation 6.1 lowers the frequency of the first acoustic modes (and the higher-frequency modes). If the excitation of this acoustic wave is in phase with the reflected signal, an instability may grow.

Chapter 7

Conclusion

For the thermoacoustic stability analysis of the hydrogen-fuelled condensing boiler, the system is modeled using CFD. The FR/EDM and UT-FGM combustion models were compared and the latter was chosen to model the reacting flow. A mesh independent, steady state solution of the combustion chamber flow field was obtained for the thermoacoustic analysis.

Different methods of determining a FTF have been compared. The transient methods, impulse and white noise excitation, resulted in comparable FTFs in gain and phase (see Figure 5.9). The FTFs are compared in an ANM modelling the condensing boiler. The obtained eigenfrequencies of the different FTFs showed an insignificant difference in the damping. All eigenfrequencies of the condensing boiler appear stable.

The LCM result did not give physical FTFs. The (normalized) gain was non-zero only for low Strouhal numbers and the phase reached a constant value rather than a constant slope representing a time delay.

7.1 RESEARCH QUESTIONS

The research subquestions can be answered:

- *Can the UT-FGM combustion model be used?* Yes, the UT-FGM combustion model is more valid for this system. The flame thickness obtained using UT-FGM was similar to the expected value based on analytical relations for the thermal flame thickness. The temperatures found were close to values found using computations in Cantera. In addition, the combustion regime of points in the flame was found to be generally in the flamelet zone, where the UT-FGM model is valid.
- *Do LCM, white noise and impulse excitation result in similar thermoacoustic eigenfrequencies?* No, LCM did not show similar frequencies as no good FTF is obtained using this method. White noise and impulse excitation did result in the same thermoacoustic eigenfrequencies.

The main research question can be answered:

> *To what extent can the LCM improve computation time and accuracy compared to white noise or impulse excitation in determining thermoacoustic stability in a hydrogen burning residential appliance?*

Without further assumptions, the used implementation of LCM with the FGM combustion model cannot be used in determining thermoacoustic stability. Under the assumption adaptations to the LCM can give accurate FTFs without significantly impacting the computation time the following statement can be made: The LCM can generate an FTF in a reduced time compared to the transient methods. Generating the coefficient matrices can be parallelized, which approximately scales the computation time by the number of parallel cores. Including the time for the order reduction, the (approximate) computation time for an identical mesh is shorter in the order of days (see Table 5.1). This difference is most significant compared to a white noise excitation simulation. The LCM results in an FTF without a time discretization error.

7.2 IMPACT OF THE RESEARCH

Stable thermoacoustic eigenfrequencies of the system have been found using the ANM. The hydrogen-fuelled condensing boiler modeled in this work can operate stably based on this analysis. The peaks seen in Figure 5.9 can result in noise at these frequencies. As sound at these frequencies is in the middle frequencies, sound damping materials may need to be included in the design of the boiler. Experimental validation can be used to identify if this is required.

In this work, advances in the development of the used modeling tools have been made: A speed improvement to the LCM code is used; the UT-FGM model required new databases for the hydrogen combustion, which have been tested in this work; and the UTA code base has been improved. These developments can be used in further research into thermoacoustic modeling.

7.3 FUTURE WORK

In this work, several points of improvement have been found. Due to time constraints, these points are not addressed here and should be considered in future work.

- The CFD simulations in this work simplify the physics which may quantitatively invalidate the results. Adiabatic walls were used to obtain the FTFs. As such, the flame is attached to the burner wall, which impacts the FTF. A lifted flame obtained when temperature boundary conditions are applied can change the FTF and consequently the stability of the system. For a quantitatively accurate result, simulations should be repeated with these conditions. The ANM should be adapted to use the correct temperature gradient in the system for the linear temperature gradient elements in the combustion chamber.

  Additionally, the effect of preferential diffusion should be examined in simulation. As the primary modes of the flame will be radial, this work assumed differential diffusion effects were negligible. This can be verified if the preferential diffusion of the reacting flow is implemented in the UT-FGM model for Ansys CFX.

  Moreover, the effect of simulating the porous medium compared to individual holes in the flame holder should be analyzed. Simulating this more accurate representation of the condensing boiler could result in different (global) flame behaviour compared to the used model settings.

- The LCM code should be reevaluated to generate FTFs using the FGM combustion model. Speed improvements with the parallelization have been made to make the 3D LCM code practical on sensible time scales. Changing the LCM source code from Matlab to a more optimized, low-level programming language (such as C++), can result in additional speed improvements.

  J.F. Kampen [38] states the computationally expensive step of computing the coefficient matrices can obtained from the CFD solver with alterations to the source code. Ansys CFX generates matrices similar to the coefficient matrices for LCM, although it does not solve the full coefficient matrices with all couplings present. If these matrices can be obtained from the solver, the most expensive step is the order reduction of the state space system.

- Experiments should be performed to validate the flow field, FTFs and the design choices for the ANM. To validate the CFD simulations, first the above changes should be made and new FTFs should be computed.

Acronyms

1D One-Dimensional. 15

ANM Acoustic Network Model. 5, 25

CFD Computational Fluid Dynamics. 1

EDM Eddy Dissipation Model. 15

FFT Fast Fourier Transform. 10, 27

FGM Flamelet Generated Manifold. 15

FR/EDM Finite Rate/Eddy Dissipation Model. 15

FTF Flame Transfer Function. 1, 9

HRR Heat Release Rate. 1, 24

LCM Linear Coefficients Method. 1, 11

PDF Probability Density Function. 16

RPV Reaction Progress Variable. 16

SST Shear Stress Transport. 13

List of symbols

ALPHABETIC

The symbols below are used in this work. The **boldfaced** symbols are vector or matrix quantities.

Δt	[s]	Time step
Δx	[m]	Grid size
$[X_i]$	[mol/m^3]	Concentration of species i
A_k	[1/s]	Reaction rate parameter in reaction k
A	[-]	Rate coefficient in EDM
$\boldsymbol{A}$	[kg/(Pa s)] OR [-]	system matrix in ANM OR Coefficient matrix in the LCM
a	[-]	Ratio of area of a duct cross-section to the perimeter
a_{ij}	[-]	Coefficient (i, j) in coefficient matrix $\boldsymbol{A}$
$\boldsymbol{B}$	[-]	Coefficient matrix in the LCM
B_k		Backward reaction rate coefficient in reaction k
b_k	[-]	Weight factor for species k
$\boldsymbol{C}$	[-]	Coefficient matrix in the LCM
C_1	[Pa s/m]	Viscous resistance coefficient
C_2	[kg/m^3]	inertial resistance coefficient
C_μ	[-]	Closure constant for $k-\varepsilon$ turbulence model ($C_\mu = 0.09$)
c	[-]	Reaction progress variable
c_0	[m/s]	speed of sound
c_p	[J/(kg K)]	Specific heat capacity at constant pressure
c_v	[-]	Reaction progress variable variance ($c_v \equiv c''^2$)
D	[-] OR [m^2/s]	Coefficient scalar in the LCM OR Mass diffusivity
D_{k_c}	[kg/(m^{3}s)]	Scalar dissipation rate of reaction progress variable
D_{k_f}	[kg/(m^{3}s)]	Scalar dissipation rate of mixture fraction
D_t	[m^2/s]	Turbulent diffusivity
E_k	[kcal/mol]	Reaction rate parameter in reaction k
F_k		Forward reaction rate coefficient in reaction k
f	[Hz] OR [-]	Frequency OR Mixture fraction (in FGM)
f_N	[Hz]	Nyquist frequency
f_v	[-]	Mixture fraction variance ($f_v \equiv f''^2$)
f_s	[Hz]	Sampling frequency
f_{turb}	[Hz]	Characteristic turbulent frequency
GR	[-]	Growth Rate
H_f	[-]	Flame transfer function
K		Number of reactions
K_{perm}	[kg/m^3]	Face permeability coefficient of a porous medium
K_{loss}	[1/m]	Head loss coefficient in a porous medium

k	[m^2/s^2]	Turbulence Kinetic Energy
L	[m]	Characteristic length
M	[kg/s]	Mass flow rate
M_f	[kg/s]	Fuel mass flow rate
M'_Q	[kg/s]	Effective mass flow rate perturbation due to HRR fluctuation
m		Number of time steps
n		Number of variables
n_c		Number of components
P_{k_c}	[kg/(m^{3}s)]	Scalar production rate of reaction progress variable
P_{k_f}	[kg/(m^{3}s)]	Scalar production rate of mixture fraction
p	[Pa]	Pressure
$\dot{Q}$	[W]	(Volume integrated) heat release rate
R	[J/(mol K)]	Universal gas constant ($R = 8.3145[J/(mol \cdot K)]$)
R_k	[mol/(m^{3}s)]	Reaction rate in reaction k
r'_{ki}		Forward rate exponent (of species i in reaction k)
r''_{ki}		Backward rate exponent (of species i in reaction k)
S_c	[kg/(m^{3}s)]	FGM chemical source term
S_i	[kg/(m^{3}s)]	Chemical source term of species i
$S_{M,x}$	[N/m^3]	Momentum source in x-direction
S_{FF}	[-]	Auto correlation of excitation F
S_{FX}	[-]	Cross correlation of excitation F and response X
S_{XX}	[-]	Auto correlation of response X
Sc_t	[-]	Turbulent Schmidt number
St	[-]	Strouhal number (non-dimensional frequency)
s_L^0	[m/s]	Laminar flame speed
T	[K]	Temperature
T_{design}	[K]	Adiabatic flame temperature at the design equivalence ratio
t	[s]	Time
U	[m/s]	Characteristic speed
u	[m/s]	Speed
$\boldsymbol{u}$	[m/s]	Velocity
u_η	[m/s]	Kolmogorov velocity scale
W_i	[kg/mol]	Molecular weight of species i
Y_i	[-]	Mass fraction of species i
x	[m]	Length

GREEK

α	[m^2/s]	Thermal diffusivity
β_k	[-]	Reaction rate parameter in reaction k
β_t	[-]	Turbulent damping coefficient
Γ_i	[m^2/s]	Molecular diffusion coefficient of species i
$\Gamma_{i_{eff}}$	[m^2/s]	Effective molecular diffusion coefficient of species i
γ	[-]	Heat capacity ratio
γ^2	[-]	Coherence
δ_L^0	[m]	Thermal flame thickness
ε	[m^2/s^3]	Turbulence Eddy Dissipation

ζ	[-]	Reduced impedance
η	[-] OR [m]	Unscaled reaction progress variable OR Kolmogorov length scale
η^b	[-]	Unscaled reaction progress variable of the burned state
η^u	[-]	Unscaled reaction progress variable of the unburned state
λ	[W/(m K)]	Thermal conductivity
μ_t	[Pa s]	Turbulent (dynamic) viscosity
ν	[m^2 /s]	Kinematic viscosity
ν'_{ki}	[-]	Forward stoichiometric coefficient (of species i in reaction k)
ν''_{ki}	[-]	Backward stoichiometric coefficient (of species i in reaction k)
ρ	[kg/m^3]	Density
ρ_0	[kg/m^3]	Mean density
τ_c	[s]	Chemical time scale
τ_k	[s]	Time at time step k
τ_t	[s]	Flow time scale
ϕ	[-]	Equivalence ratio
ϕ_{design}	[-]	Mean equivalence ratio of the condensing boiler
ϕ_{st}	[-]	Stoichiometric equivalence ratio
Ψ		Vector of independent variables
ψ	[-]	Friction factor
ψ_i		Independent variable i
ω	[rad/s]	Frequency
ω_i	[rad/s]	Imaginary component of frequency
$\dot{\omega}_k$	[kg/(m^3s)]	Mass production rate of species k
ω_r	[rad/s]	Real component of frequency

NOTATION

The brackets () below are a placeholder for a symbol.

$()_0$	Mean flow
$()_{design}$	Design specification
$\overline{()}$	Normalized OR Averaged
$()'$	Perturbation
exp()	Exponential (base $e \approx 2.718$)
$\boldsymbol{I}$	Identity matrix

List of non-dimensional quantities

Symbol	Equation	Name	Meaning
Da	$\frac{k}{\varepsilon}\frac{s_L^0}{\delta_L}$	Damköhler	ratio of the turbulent macro mixing timescale to the chemical time scale
Ka	$\sqrt{\frac{\varepsilon}{\nu}}\frac{\delta_L}{s_L^0}$	Karlovitz	ratio of chemical time scale to turbulent micro mixing time scale
Le	$\frac{\alpha}{D}$	Lewis	Ratio of thermal diffusivity to mass diffusivity
Ma	$\frac{u}{c_0}$	Mach	Ratio of the local flow velocity to the speed of sound
Re	$\frac{\rho u L}{\mu}$	Reynolds	Ratio of inertial forces to viscous forces in the momentum equation
Re_t	$\frac{\nu_t}{\nu}$	Turbulent Reynolds	Ratio of turbulent kinematic viscosity to laminar kinematic viscosity
Sc	$\frac{\nu}{D}$	Schmidt	Ratio of viscous diffusion to mass diffusion
Sc_t	$\frac{\nu_t}{K_t}$	Turbulent Schmidt	Ratio of turbulent transport of momentum to turbulent transport of mass
St	$\frac{fL}{u}$	Strouhal	Ratio of oscillating frequency to the characteristic frequency

Appendix A

Mesh sensitivity study

The computational domain of the hydrogen burner was divided into three subdomains as shown in Figure A.1. Domain 1 starts after the fan and simulates a large part of the mixing chamber.

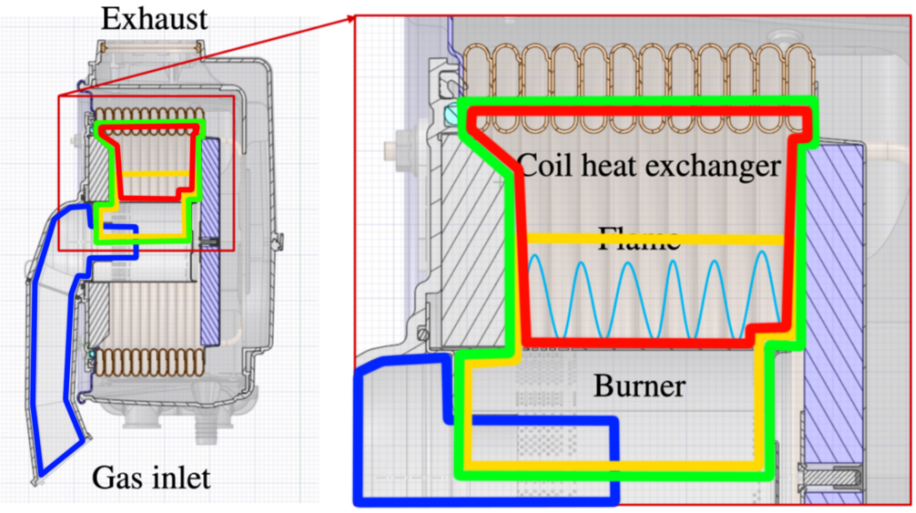

Figure A.1: Division of the system in computational domains (superposed on Figure 1.1). Domain 1 (blue) is for the mixing simulation; Domain 2 (green) is for the combustion chamber inlet conditions; Domain 3 (yellow) is for verification of the distribution obtained using Domain 2; Domain 4 (red) is the combustion chamber used to generate the FTFs.

Different turbulence intensities at the inlet were simulated and the results were compared. As the difference in flow pattern and mixing was small, an inlet turbulence intensity of 10% was used to reflect the high turbulence intensity after the fan. The bulk of the domain was meshed with tetrahedral cells and an inflation layer at the walls was applied to achieve a y^+-value of approximately 1, as required for the k-ω SST turbulence model used for the initial simulations.

In this simulation, mixing of the air with the fuel was considered. The isothermal simulation of Domain 1 is performed at normal temperature and pressure (20°C; 1 atm) [17]. Flow conditions, such as velocity and turbulence parameters, were exported from a slice of the domain upstream of the point of mixing. These results were used as the inlet conditions for Domain 2. Domain 2 therefore has overlap in the geometry with Domain 1. This choice was made to consider the upstream effects of the mixing geometry in Domain 1.

Domain 2 contains part of the mixing chamber, a flame holder modeled as a porous zone, and

the combustion chamber. As the flow in the cross-sectional plane used for the inlet of Domain 2 was near axisymmetric and the domain has radial symmetry, a slice of the full domain is used to reduce the computational effort. Periodic boundary conditions are applied to the radial boundary planes. Simulation of Domain 2 included energy transport and combustion. As such, to capture large gradients in the combustion chamber at the flame location, the mesh was refined locally.

To evaluate the grid dependency of Domain 2, a subdomain that included the porous zone was simulated to compare the mixing and velocity distribution. This subdomain was evaluated on 3 different grids. The resulting equivalence ratio and velocity distributions on the porous zone were compared with the result from Domain 2, showing comparable results. This simulation included energy transport and combustion, similar to the simulation of Domain 2.

A more detailed sensitivity study is performed on the combustion chamber domain. A flame has high gradients (for temperature, species mass fraction, etc.) that need to be captured accurately. If the element size is too large in this region, the result can be inaccurate. Conversely, if the element size is too small, the domain has too many elements, which will slow down the simulation. As the remainder of the combustion chamber is relatively simple, the main grid refinement occurs at the flame front. The solution in the remainder of the domain was found to be grid independent for a relatively coarse element size. Similar to Domain 2, a periodic slice of the domain was used for the initial simulation of the combustion chamber. The solution appeared symmetric along the bisector plane, so a smaller slice of the combustion chamber is used with imposed symmetry boundary conditions on the radial planes. This reduction in domain size allows for the use of smaller elements with comparable simulation time.

In Section 4.1.2, two combustion models are compared. It was found the two models result in different flame lengths. As such, different meshes have to be used, due to the highly local refinement of the flame front. In the comparison, mesh independent results are needed, therefore two mesh sensitivity studies are performed. For obtaining the flame transfer function, the main result of the computation is the heat release rate. As such, this was used as the primary parameter to determine the grid independence.

A.1 FINITE RATE/EDDY DISSIPATION MODEL SENSITIVITY STUDY

The FR/EDM combustion model resulted in a flame front wider than the thermal thickness given identical conditions. As such, coarser elements can be used for this flame, although a larger region in the domain requires the mesh refinement compared to the FGM model. In Figure A.2, the normalized heat release rate of the different (normalized) grid sizes is shown. The heat release rate is normalized by the ideal value at infinitesimally small grid size. The element size is normalized by the thermal flame thickness. The error in heat release rate in the flame region is less than 1% for a grid size of $\Delta\overline{x} = 0.88$ and smaller. The change in heat release rate behaves quadratic in the cell size, as expected from the high resolution advection scheme used.

When considering the maximum temperature in the domain, a difference can be seen for the largest cell size simulated (see Figure A.3). The temperature is normalized with the adiabatic flame temperature at the design equivalence ratio ϕ_{design}. For the largest grid size ($\Delta\overline{x} > 1$), the maximum temperature deviates significantly from the other finer meshes. As such, this mesh is not used for the comparison.

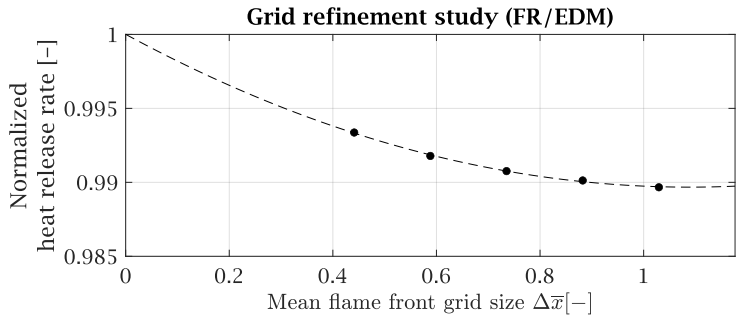

Figure A.2: Volume integrated, normalized heat release rate for various mean flame front element sizes. The simulations use the Finite Rate/Eddy Dissipation Model to model combustion. A quadratic curve (dashed line) is fitted on the data.

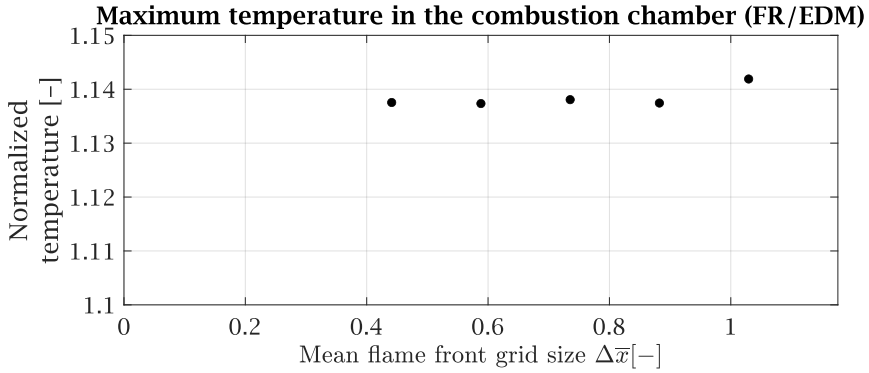

Figure A.3: Maximal temperature with grid refinement for the symmetric slice of the combustion chamber (using Finite Rate/Eddy Dissipation Model).

The final choice in grid was made based on the temperature, species mass fractions and radial velocity distribution in various points near the flame region[1]. The coarse grids ($\Delta\overline{x} \geq 1$) showed to deviate significantly from the finer meshes. The mesh with mean flame grid size of $\Delta\overline{x} = 0.88$ was chosen for the comparison. The mass fraction distribution correspond well with the more refined meshes and the normalized HRR is less than 1%.

A.2 FLAMELET GENERATED MANIFOLD SENSITIVITY STUDY

The sensitivity study is repeated for the FGM combustion model. The flame front is thinner compared to FR/EDM, consequently requiring finer elements in the flame front region. The heat release rate found using this combustion model is shown in Figure A.4. Compared to FR/EDM, the error in HRR is greater for FGM by an order of magnitude (for $\Delta\overline{x} = 0.44$, the FR/EDM error is 0.7% and the FGM error is 7.5%). Again, the HRR converges quadratically to an ideal value (used to normalize the HRR). From Figure A.5, it becomes clear the maximum temperature is very similar for all considered mean flame front grid sizes. As such, this measure cannot be used to exclude a mesh from the analysis.

[1]Not shown for reasons of confidentiality.

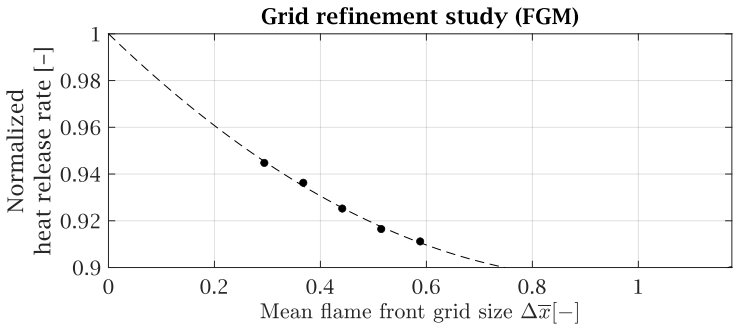

Figure A.4: Volume integrated, normalized heat release rate for various mean flame front element size. The simulations use the Flamelet Generated Manifold model to model combustion. A quadratic curve (dashed line) is fitted on the data.

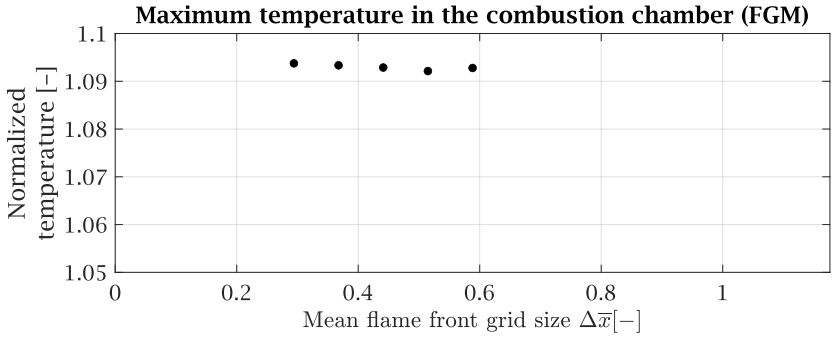

Figure A.5: Maximal temperature with grid refinement for the symmetric slice of the combustion chamber (using Flamelet Generated Manifold model).

The main parameter in determining the mesh used is the shape of the flame. Only the $\Delta\overline{x} \leq 0.36$ grids have a V-shaped flame along the flame front. Results of simulations on the other meshes show a collapsed flame tip (see Figure A.6). As the smaller element size generates this V-shaped tip (expected for a near laminar flame), the coarser meshes are disregarded. The error in HRR is 6.4%, which is high compared to the FR/EDM result. The finest mesh was not used, as the cell count would have slowed the transient simulations excessively.

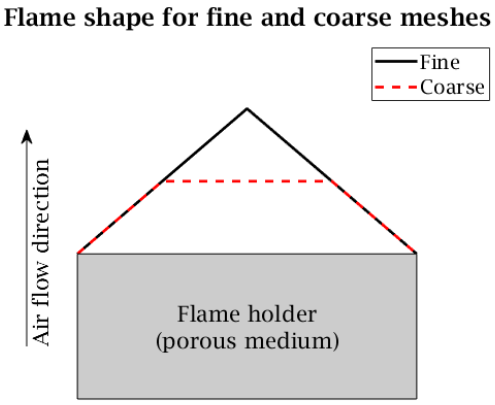

Figure A.6: Schematic overview of collapsed flame tip observed in the coarse meshes compared to finer meshes. From the grey box representing the flame holder, the flame in the simulations with fine grids ($\Delta\overline{x} \leq 0.36$) form a V-shaped flame (black line). The other grids result in a flattened flame tip (dashed red line).

Appendix B

Porous zone modeling

The burner wall contains small holes for the fuel/air mixture to pass through. Flow is accelerated in these perforations to exceed the flame speed due to the area contraction. As such, the risk of flashback is reduced. The diameter of these holes is in the order of δ_L^0. Consequently, this geometry is too complex to resolve with a grid [3]. Rather, a porous medium is employed to model the flow in this region of the domain. The medium should capture the pressure drop across the holes, such that the upstream flow field is unaffected.

In Ansys CFX5, porous media can be modeled as a fluid region with additional porosity parameters. Porous zones act as a momentum sink to find a pressure drop based on Darcy's law [2, 41]. The pressure drop Δp increases for increasing flow speed u:

$$\Delta p = C_1 u + C_2 u^2 + H.O.T. \tag{B.1}$$

Here, C_1 and C_2 are modeling coefficients called viscous resistance coefficient and inertial resistance coefficient, respectively[1]. Higher order terms are neglected. C_1 includes viscous effects and a permeability parameter as $C_1 = \frac{\mu}{K_{perm}}$. C_2 includes inertial effects and a loss parameter as $C_2 = K_{loss}\frac{\rho}{2}$. The source term in the momentum equation in x-direction becomes [3]:

$$S_{M,x} = -\frac{\mu}{K_{perm}} u - K_{loss}\frac{\rho}{2}|\boldsymbol{u}|u \tag{B.2}$$

Determining these coefficients can be done using different methods. As empirical data is not available for the geometry of the residential boiler, the different methods are covered briefly in the following sections. These methods are used for the streamwise loss; the transverse loss is obtained by multiplying the streamwise loss with a sufficiently high coefficient (1000 in this work[2]). The flow after the porous zone is radially outward due to this coefficient multiplier.

To approximate the effects of the perforated plate on the turbulence, the turbulence intensity is set to low in the combustion chamber CFD simulations. The most energetic eddies are dissipated by the plate as in [6], and the Reynolds number in the porous zone is low.

[1] In Ansys CFX, these coefficients are the linear and quadratic resistance coefficients [3].

[2] If this value is too high, the momentum sink might be too great, resulting in convergence problems. If the coefficient multiplier is chosen too low, the flow will have too much transverse momentum and the flow field will be affected.

BERNOULLI EQUATION APPROXIMATION

As a crude approximation of the pressure drop, the inviscid, incompressible Bernoulli equation can be used (ignoring gravity):

$$\frac{u^2}{2} + \frac{p}{\rho} = \text{constant} \tag{B.3}$$

Here, u is the flow speed, p is the (static) pressure and ρ is the density. By considering the difference in flow speed, a pressure drop approximation can be determined. Equation B.3 is rewritten to:

$$\Delta p = \frac{1}{2}\rho\left(u_1^2 - u_0^2\right) \tag{B.4}$$

Here, u_1 is the accelerated flow speed and u_0 is the flow speed before the constriction. This method provides an approximate pressure drop in the order of magnitude expected. This value can be compared against the other methods.

DATA FROM ENGINEERING HANDBOOKS

Experimental data can be approximated using values from textbooks. The relevant geometry can be found and the coefficients can be interpolated from existing data. The 'Thickened grid (perforated plate or laths)' data from Idel'Chik [14] is used to find C_2 (also known as the head loss coefficient). The thickened grid tables were chosen as the length over diameter of the burner geometry is near unity. For this table, the open area ratio, the plate thickness to hole diameter ratio and orifice friction factor are considered. A resistance coefficient is computed which is converted to a loss coefficient K_{loss} by dividing by the thickness of the material.

CFD APPROACH

Instead of incorporating the perforations in the full geometry, which is impractical, an individual hole can be modeled to find the pressure drop across the burner wall. For different flow speeds normal to the hole, the hole can be simulated using a CFD solver. The $k-\omega$ SST turbulence model is used and the pressure drop is obtained for the different inlet conditions. The pressure drop can be found by integrating the frictional forces over the wall in the isothermal simulations. A second order polynomial can be fitted to find the coefficients C_1 and C_2 (from Equation B.1).

CONCLUDING REMARKS

The resulting linear and quadratic resistance coefficients can be compared to the result from the engineering handbook. The two methods matched closely. The CFD approach is used to find the values for the model settings of the porous zone. These results are in the order of magnitude found by the bernoulli equation approximation.

List of References

[1] Eirik Æsøy et al. “Tailoring the Gain and Phase of the Flame Transfer Function through Targeted Convective-Acoustic Interference”. In: *Combustion and Flame* 236 (Feb. 2022), p. 111813. ISSN: 00102180. DOI: 10.1016/j.combustflame.2021.111813. (Visited on 11/04/2024).

[2] ANSYS. *ANSYS Fluent - CFD Software | ANSYS*. 2016. URL: http://www.ansys.com/products/fluids/ansys-fluent.

[3] ANSYS. *ANSYS CFX - Solver Theory Guide*. 2023. URL: https://www.ansys.com/products/fluids/ansys-cfx.

[4] Alexander Avdonin, Max Meindl, and Wolfgang Polifke. “Thermoacoustic Analysis of a Laminar Premixed Flame Using a Linearized Reactive Flow Solver”. In: *Proceedings of the Combustion Institute* 37.4 (2019), pp. 5307–5314. ISSN: 15407489. DOI: 10.1016/j.proci.2018.06.142. (Visited on 04/08/2024).

[5] Harmen De Vries, Anatoli V. Mokhov, and Howard B. Levinsky. “The Impact of Natural Gas/Hydrogen Mixtures on the Performance of End-Use Equipment: Interchangeability Analysis for Domestic Appliances”. In: *Applied Energy* 208 (Dec. 2017), pp. 1007–1019. ISSN: 03062619. DOI: 10.1016/j.apenergy.2017.09.049.

[6] Moussa Diop et al. “Experimental and Numerical Investigation of the Diffusion of a Confined Wall Jet through a Perforated Plate”. In: *Open Journal of Fluid Dynamics* 12.02 (2022), pp. 168–212. ISSN: 2165-3852, 2165-3860. DOI: 10.4236/ojfd.2022.122009. (Visited on 04/23/2024).

[7] Abdulla Ghani and Wolfgang Polifke. “Control of Intrinsic Thermoacoustic Instabilities Using Hydrogen Fuel”. In: *Proceedings of the Combustion Institute* 38.4 (2021), pp. 6077–6084. ISSN: 15407489. DOI: 10.1016/j.proci.2020.06.151. (Visited on 01/24/2024).

[8] Paul Glanville et al. “Impact of Hydrogen/Natural Gas Blends on Partially Premixed Combustion Equipment: NOx Emission and Operational Performance”. In: *Energies* 15.5 (Feb. 2022), p. 1706. ISSN: 1996-1073. DOI: 10.3390/en15051706.

[9] David G. Goodwin et al. *Cantera: An Object-oriented Software Toolkit for Chemical Kinetics, Thermodynamics, and Transport Processes*. https://www.cantera.org. Version 3.0.0. 2023. DOI: 10.5281/zenodo.8137090.

[10] David G. Goodwin et al. *Cantera: Python tutorial*. https://cantera.org/tutorials/python-tutorial.html. Accessed: 26-09-2024. 2023.

[11] Harish S. Gopalakrishnan, Andrea Gruber, and Jonas Moeck. “Computation of Intrinsic Instability and Sound Generation From Auto-Ignition Fronts”. In: *Journal of Engineering for Gas Turbines and Power* 145.4 (Apr. 2023), p. 041008. ISSN: 0742-4795, 1528-8919. DOI: 10.1115/1.4055421. (Visited on 01/26/2024).

[12] Simon Gövert. "Modelling the Effects of Heat Loss and Fuel/Air Mixing on Turbulent Combustion in Gas Turbine Combustion Systems". PhD thesis. Enschede, The Netherlands: University of Twente, Dec. 2016. ISBN: 9789036542449. DOI: 10.3990/1.9789036542449. (Visited on 09/19/2024).

[13] Jesse W. Hofsteenge, Alireza Ghasemi Khourinia, and Jim B. W. Kok. "Numerical Simulations of Heat Loss Effect on Premixed Jet Flame Using Flamelet Generated Manifold Combustion Model". In: *Energies* 15.3 (Jan. 2022), p. 730. ISSN: 1996-1073. DOI: 10.3390/en15030730.

[14] I. E. Idelchik and M. O. Steinberg. *Handbook of hydraulic resistance*. Boca Raton, FL: CRC Press, 1994.

[15] Intel. *Intel® Xeon® Gold 6140 processor (24.75m Cache, 2.30 GHz) - product specifications*. Accessed: 11-10-2024. URL: https://www.intel.com/content/www/us/en/products/sku/120485/intel-xeon-gold-6140-processor-24-75m-cache-2-30-ghz/specifications.html.

[16] Intel. *Intel® Xeon® processor E7-8890 V4 (60m Cache, 2.20 GHz) - product specifications*. Accessed: 11-10-2024. URL: https://www.intel.com/content/www/us/en/products/sku/93790/intel-xeon-processor-e78890-v4-60m-cache-2-20-ghz/specifications.html.

[17] ISO International Organization for Standardization. *Geometrical product specifications (GPS) — Standard reference temperature for the specification of geometrical and dimensional properties*. Standard. Geneva, CH: International Organization for Standardization, June 2022.

[18] Hyebin Kang and Kyu Tae Kim. "Combustion Dynamics of Multi-Element Lean-Premixed Hydrogen-Air Flame Ensemble". In: *Combustion and Flame* 233 (Nov. 2021), p. 111585. ISSN: 00102180. DOI: 10.1016/j.combustflame.2021.111585. (Visited on 01/26/2024).

[19] Robert Kee et al. "A Fortran Computer Code Package For The Evaluation Of Gas-Phase, Multicomponent Transport Properties". In: (Aug. 1996).

[20] Pieter Kroon. *Waterstofverbranding en stikstofemissies*. TNO 2023 R10343 | Eindrapport. TNO, Apr. 2023.

[21] Jeffrey C. Lagarias et al. "Convergence Properties of the Nelder–Mead Simplex Method in Low Dimensions". In: *SIAM Journal on Optimization* 9.1 (1998), pp. 112–147. DOI: 10.1137/S1052623496303470. URL: https://doi.org/10.1137/S1052623496303470.

[22] HsuChew Lee et al. "Influence of Equivalence Ratio on Turbulent Burning Velocity and Extreme Fuel Consumption Rate in Lean Hydrogen-Air Turbulent Flames". In: *Fuel* 327 (Nov. 2022), p. 124969. ISSN: 00162361. DOI: 10.1016/j.fuel.2022.124969. (Visited on 10/30/2024).

[23] Jörg Leicher et al. "The Impact of Hydrogen Admixture into Natural Gas on Residential and Commercial Gas Appliances". In: *Energies* 15.3 (Jan. 2022), p. 777. ISSN: 1996-1073. DOI: 10.3390/en15030777.

[24] Timothy Charles Lieuwen. *Investigation of combustion instability mechanisms in premixed gas turbines*. Georgia Institute of Technology, 1999.

[25] Ennio Giovanni Luciano and Javier Manuel Ballester Castañer. "Flame Transfer Function: description, interpretation and use for prediction and control of thermoacoustic instabilities in premixed methane and biogas flames". PhD thesis. Universidad de Zaragoza, 2021.

[26] Joaquim R. R. A. Martins and Andrew Ning. *Engineering Design Optimization*. Cambridge, UK: Cambridge University Press, Jan. 2022. ISBN: 9781108833417. DOI: 10.1017/9781108980647. URL: https://mdobook.github.io.

[27] Aimee Morgans. *OSCILOS: The open source combustion instability low order simulator*. 2014. URL: https://www.oscilos.com/index.html.

[28] Nithin Mukundakumar et al. "A New Preferential Diffusion Model Applied to FGM Simulations of Hydrogen Flames". In: *Combustion Theory and Modelling* 25.7 (Nov. 2021), pp. 1245–1267. ISSN: 1364-7830, 1741-3559. DOI: 10.1080/13647830.2021.1970232. (Visited on 02/08/2024).

[29] Nefit Bosch. *Energiezuinige cv-ketel voor comfortabele verwarming en warmwatercomfort*. Accessed on: 31-11-2024. 2024. URL: https://www.nefit-bosch.nl/producten/cv-ketels#vermogen.

[30] Jeroen van Oijen and Philip Goey. "Modelling of Premixed Laminar Flames using Flamelet-Generated Manifolds". In: *Combustion Science and Technology - COMBUST SCI TECHNOL* 161 (Dec. 2000), pp. 113–137. DOI: 10.1080/00102200008935814.

[31] N. Peters. "Laminar Flamelet Concepts in Turbulent Combustion". In: *Symposium (International) on Combustion* 21.1 (Jan. 1988), pp. 1231–1250. ISSN: 00820784. DOI: 10.1016/S0082-0784(88)80355-2. (Visited on 09/27/2024).

[32] T. Poinsot and D. Veynante. *Theoretical and Numerical Combustion*. Edwards, 2005. ISBN: 9781930217102.

[33] Wolfgang Polifke. *taX software*. 2014. URL: https://www.epc.ed.tum.de/en/tfd/research/tax-software/.

[34] Wolfgang Polifke. "Modeling and Analysis of Premixed Flame Dynamics by Means of Distributed Time Delays". In: *Progress in Energy and Combustion Science* 79 (July 2020), p. 100845. ISSN: 03601285. DOI: 10.1016/j.pecs.2020.100845. (Visited on 06/24/2024).

[35] Thierry Schuller, Thierry Poinsot, and Sébastien Candel. "Dynamics and Control of Premixed Combustion Systems Based on Flame Transfer and Describing Functions". In: *Journal of Fluid Mechanics* 894 (July 2020), P1. ISSN: 0022-1120, 1469-7645. DOI: 10.1017/jfm.2020.239. (Visited on 11/04/2024).

[36] John Strollo, Stephen Peluso, and Jacqueline O'Connor. "Effect of Hydrogen on Steady-State and Transient Combustion Instability Characteristics". In: *Journal of Engineering for Gas Turbines and Power* 143.7 (July 2021), p. 071023. ISSN: 0742-4795, 1528-8919. DOI: 10.1115/1.4049481. (Visited on 08/12/2024).

[37] Stuurgroep NP-H2IGO. *Slotpublicatie NP-H2IGO*. Normalisatieplatform H2 Industrie en Gebouwde omgeving. NEN, Jan. 2024.

[38] J.F. van Kampen. "Acoustic pressure oscillations induced by confined turbulent premixed natural gas flames". English. PhD Thesis - Research UT, graduation UT. Netherlands: University of Twente, Mar. 2006. ISBN: 90-365-2277-3. DOI: 10.3990/1.9789036522779.

[39] J.A. Van Oijen, F.A. Lammers, and L.P.H. De Goey. "Modeling of Complex Premixed Burner Systems by Using Flamelet-Generated Manifolds". In: *Combustion and Flame* 127.3 (Nov. 2001), pp. 2124–2134. ISSN: 00102180. DOI: 10.1016/S0010-2180(01)00316-9. (Visited on 10/30/2024).

[40] Haifeng Wang and Tianfang Xie. *Stoichiometry Preservation and Generalization of Bilger Mixture Fraction for Non-Premixed Combustion with Differential Molecular Diffusion*. Dec. 2023. eprint: 2312.05204 (physics). (Visited on 06/27/2024).

[41] Aidan Wimhurst. *[CFD] Porous zones in CFD*. Accessed: 04-11-2024. Sept. 2019. URL: https://www.fluidmechanics101.com/.

[42] Anthony Young. *The Saturn V F-1 Engine: Powering Apollo into History*. Berlin: Springer published in association with Praxis publ, 2009. ISBN: 978-0-387-09629-2.

[43] Dan Zhao. "Chapter 1 - Introduction of self-sustained thermoacoustic instability". In: *Thermoacoustic Combustion Instability Control*. Ed. by Dan Zhao. Academic Press, 2023, pp. 1–112. ISBN: 978-0-323-89910-9. DOI: https://doi.org/10.1016/B978-0-323-89910-9.00011-9. URL: https://www.sciencedirect.com/science/article/pii/B9780323899109000119.